

# **IDEA** League

MASTER OF SCIENCE IN APPLIED GEOPHYSICS  
RESEARCH THESIS

---

**Using reflected seismic waves to  
estimate rheological properties of the  
fluid-mud layer for port applications**

**George Woofenden**

---

August 10, 2017



# **Using reflected seismic waves to estimate rheological properties of the fluid-mud layer for port applications**

MASTER OF SCIENCE THESIS

for the degree of Master of Science in Applied Geophysics

by

George Woofenden

August 10, 2017



IDEA LEAGUE  
JOINT MASTER'S IN APPLIED GEOPHYSICS

Delft University of Technology, The Netherlands  
ETH Zürich, Switzerland  
RWTH Aachen, Germany

Dated: *August 10, 2017*

Supervisor(s):

---

Dr. Deyan Draganov

---

Alex Kirichek

Committee Members:

---

Dr. Deyan Draganov

---

Alex Kirichek

---

Prof. Florian Wellman



---

# Abstract

Current Port of Rotterdam procedure is to define the nautical depth based on the density of a fluid-mud layer, that settles at the bottom of the port. Rheological parameters could be an improved indicator for nautical depth and decrease the frequency and cost of dredging. I investigate the use of reflected seismic waves to derive in situ rheological parameters. I model a simplified port profile to investigate the effects of offset on the types of seismic reflections acquired. Four models of how the density of the fluid-mud layer varies with depth are proposed. I undertake simple laboratory experiments to measure the effects of consolidation time, density and frequency has on the seismic velocities of the fluid-mud layer. From these laboratory experiments I calculate the shear modulus, bulk modulus, Young's modulus and Poisson's ratio for the fluid-mud layer of varying densities. Reflected seismic-wave velocities prove to be promising in deriving in situ rheological parameters, elastic constants and, potentially, viscosity.



---

# Acknowledgements

First of all, I want to thank all the people who have participated in this project with me. Namely: Alex Kirichek, Deyan Draganov and Karel Heller. Thanks to my family for being so supportive and for getting me to where I am today. I would also like to acknowledge all the members of Rugby Club Delft for being like a family to me during my time in the Netherlands, I will not forget the times I have had and friends I have made. I would like to especially mention Rogier van Damme for helping me feel settled and giving me a job during my time in Delft. I would also like to extend this thanks to the crew at De Beierd, I have thoroughly enjoyed working my Friday night shifts there and it is an honour to work with such a nice team. I also cannot praise Mara Verhoeff and her family enough for helping me out during my first month in Delft. Ushi and Joost were genuinely the most generous hosts and I have never eaten so well in my life ! Lastly I would like to take the opportunity to thank and praise all my fellow peers on the IDEA league course, I couldn't think of any better people to study and explore Europe together. May we have many more good times ahead !

Delft University of Technology, The Netherlands  
August 10, 2017

George Woofenden



---

# Table of Contents

<b>Abstract</b>	<b>v</b>
<b>Acknowledgements</b>	<b>vii</b>
<b>Acronyms</b>	<b>xvii</b>
<b>I Introduction</b>	<b>1</b>
1 Introduction	3
<b>II Theory</b>	<b>7</b>
2 Scholte Wave	9
2-1 Introduction . . . . .	9
2-2 Theory - Isotropic Medium . . . . .	9
2-3 Theory - Two Isotropic Half-spaces . . . . .	12
2-4 Use for parameter determination . . . . .	14
2-4-1 Shear Modulus . . . . .	17
2-4-2 Bulk Modulus . . . . .	17
2-4-3 Elastic Constants . . . . .	19
<b>III Modelling</b>	<b>21</b>
3 Modelling	23
3-1 The Effects of Source and Receiver Height above the Fluid-Mud . . . . .	23
3-2 Velocity Determination . . . . .	24
3-3 Shear and Bulk Modulus . . . . .	26
3-4 Elastic Parameters . . . . .	28

<b>IV</b>	<b>Laboratory Experiments</b>	<b>35</b>
<b>4</b>	<b>Laboratory Experiments</b>	<b>37</b>
4-1	Introduction . . . . .	37
4-2	Velocity Measurements of PoR fluid-mud of varying density. . . . .	37
4-2-1	Introduction . . . . .	37
4-2-2	Laboratory Setup . . . . .	38
4-2-3	Methodology . . . . .	39
4-3	The effects of frequency on wave velocity for the PoR fluid-mud. . . . .	39
4-3-1	Introduction . . . . .	39
4-3-2	Laboratory Setup . . . . .	40
4-3-3	Methodology . . . . .	40
4-4	Effects of time on the seismic/rheological properties of PoR fluid-mud . . . . .	40
4-4-1	Introduction . . . . .	40
4-4-2	Laboratory Setup . . . . .	40
4-4-3	Methodology . . . . .	41
<b>V</b>	<b>Results</b>	<b>43</b>
<b>5</b>	<b>Results</b>	<b>45</b>
5-1	Velocity - Density . . . . .	45
5-2	Velocity - Frequency . . . . .	46
5-3	Velocity - Time . . . . .	46
<b>VI</b>	<b>Discussion</b>	<b>53</b>
<b>6</b>	<b>Discussion</b>	<b>55</b>
6-1	Modelling . . . . .	55
6-2	Velocity Measurements . . . . .	56
6-3	Frequency Measurements . . . . .	56
6-4	Effects of time on the seismic and rheological properties of fluid-mud . . . . .	57
6-4-1	P-Wave Velocity . . . . .	57
6-4-2	S-Wave Velocity . . . . .	57
6-4-3	Density . . . . .	57
6-4-4	Fluid-mud Interface . . . . .	58
6-4-5	Reflection Coefficient . . . . .	58
6-4-6	Shear & Bulk Modulus . . . . .	59
6-4-7	Elastic Constants . . . . .	59
6-5	Further Research . . . . .	60
6-5-1	Viscosity Determination . . . . .	60

<b>Table of Contents</b>	<b>xi</b>
<b>VII Conclusion</b>	<b>61</b>
<b>7 Conclusion</b>	<b>63</b>
<b>Bibliography</b>	<b>65</b>

---



---

# List of Figures

1-1	Fluid-mud settling and bed formation in inactive water Mehta et al. (2014). . . . .	4
1-2	Relationship of Shear Strength to Mud Density for many ports Fontein and van der Wal (2006). . . . .	4
1-3	Schematic of the field setup for the MASW method. Park et al. (2005). . . . .	6
2-1	Excited Scholte Wave at a fluid-solid interface. Bohlen et al. (2004). . . . .	9
2-2	How the Scholte wave velocity varies with S-wave velocity and density. . . . .	16
2-3	How the Scholte wave velocity varies with S-wave velocity and P-Wave velocity. . . . .	17
2-4	How the shear modulus varies with a change in Scholte wave (blue) and S-wave velocity (green) for a fluid-mud density of $1200 \text{ kg.m}^3$ . . . . .	18
2-5	Squared velocity ratio against the inverse shear modulus for a density of the fluid-mud of $1200 \text{ kgm}^{-3}$ . The gradient of the plot is equal to the bulk modulus. . . . .	18
3-1	The model parameters used in the 3 layer model. P-wave velocity (Blue), S-wave velocity (Red) and Density (Green). . . . .	24
3-2	Modelled seismic response with an offset of 10 m . . . . .	25
3-3	Modelled seismic response with an offset of 5 m . . . . .	25
3-4	Modelled seismic response with an offset of 2 m . . . . .	26
3-5	Modelled seismic response with an offset of 1 m . . . . .	26
3-6	Modelled seismic response with an offset of 0.5 m . . . . .	27
3-7	Modelled seismic response with an offset of 0.2 m . . . . .	27
3-8	How the shear modulus varies for low Scholte-wave (blue) and S-wave (green) velocities for a fluid-mud density of $1200 \text{ kg.m}^{-3}$ . . . . .	28
3-9	The four models of how the density varies with depth for fluid-mud. . . . .	29
3-10	The four models of how the shear modulus varies with depth for fluid-mud. . . . .	30
3-11	The three models of how the Shear modulus varies with density for fluid-mud. . . . .	31
3-12	The three models of how the S-wave velocity varies with depth for fluid-mud. . . . .	31

3-13	The four models of how the Bulk modulus varies with depth for the fluid-mud layer	32
3-14	The four models of how the Young's modulus varies with depth for fluid-mud. . .	32
3-15	The four models of how the Lamé's first parameter varies with depth for fluid-mud.	33
3-16	The four models of how the Poission ratio varies with depth for fluid-mud. . . . .	33
3-17	The four models of how the P-wave modulus varies with depth for fluid-mud. . .	34
4-1	The location (red box) of 8e Petroleumhaven in the PoR of which the fluid-mud sample is taken from. . . . .	38
4-2	The laboratory setup for P-wave and S-wave velocity investigation. . . . .	39
5-1	The results of the velocity measurements on the PoR fluid-mud of varying density.	45
5-2	The results of the velocity measurements on the PoR fluid-mud of varying frequency.	46
5-3	The results of the P-wave velocity measurements on the PoR fluid-mud with increasing time. . . . .	47
5-4	The results of the S-wave velocity measurements on the PoR fluid-mud with increasing time. . . . .	47
5-5	A graph to show how density changes with time for the PoR fluid-mud. . . . .	48
5-6	A graph to show how P-wave reflection coefficient changes with time for the PoR fluid-mud. . . . .	48
5-7	A graph to show how the shear and bulk modulus change with time for the PoR fluid-mud. . . . .	49
5-8	A graph to show how the shear and bulk modulae change with density for the PoR fluid-mud. . . . .	49
5-9	A graph to show how the Young's modulus changes with density for the PoR fluid-mud. . . . .	50
5-10	A graph to show how the Poisson's ratio changes with density for the PoR fluid-mud.	50
5-11	A graph to show how the first Lamé parameter changes with density for the PoR fluid-mud. . . . .	51
6-1	A graph to show how the height of the PoR fluid-mud interface changes with time. Red = stage 1, Yellow = stage 2 and Green = stage 3. . . . .	59

---

# List of Tables

2-1	Table of Parameters. . . . .	10
2-2	A table of elastic constants derived from the Bulk and Shear modulus for a isotropic, linear elastic medium. . . . .	19
3-1	A table of elastic constants from the modelled data. . . . .	28



---

# Acronyms

**DUT** Delft University of Technology

**ETH** Swiss Federal Institute of Technology

**RWTH** Aachen University

**PoR** Port of Rotterdam



## **Part I**

# **Introduction**



---

# Chapter 1

---

## Introduction

The task of maintaining waterways for safe navigation within ports is typically expensive and inefficient. Fluid-like sediments deposited by tides, river flow and waves must be monitored and managed to ensure ships can move safely through the port. These fluid-like sediments, referred to as "fluid-mud" from here on, are characterized by their low density and shear strength. Fluid-mud is defined as "Cohesive fine-grained sediment suspension with a concentration below that required for soil formation", [Fontein and van der Wal \(2006\)](#). Current port practices at the Port of Rotterdam (PoR) define the nautical-depth as the depth at which this fluid-mud has a density of  $1.2 \text{ kgm}^{-3}$ , ([McAnally et al. \(2007\)](#)).

Fluid-mud is formed from a dilute suspension in either still or flowing water, as a result of wave action or mechanical agitation of a settled sediment bed. Fluid-mud will form if the flux of sediment deposited inside the layer of water above the bed exceeds the rate at which fluid-mud is settling (dewatering) on the sediment bed. Hence, fluid-mud will only grow in thickness if the flux of sediment settling onto the bed exceeds the rate at which fluid-mud dewateres. This is demonstrated for still water in [Figure 1-1](#).

Using the density of the fluid mud as a definition is a practical solution, but it is a simplification of nautical-depth. [Fontein and van der Wal \(2006\)](#) suggested that adopting a new definition of nautical depth may reduce maintenance costs. The rheological properties of the fluid-mud provide direct parameters influencing ship navigation. Such rheological properties to be investigated include shear strength and viscosity. If the in-situ rheological properties of the fluid-mud can be accurately determined, this could allow the charted depth to be guaranteed whilst decreasing the frequency of fluid-mud dredging, ultimately decreasing the maintenance costs for the port authorities. [Figure 1-2](#) highlights the fact that a single nautical depth does not exist for ports worldwide. This is not better demonstrated than by the relationship between the shear strength and density for fluid-mud in Guyana. Even at a density of  $1.5 \text{ kgm}^{-3}$  the shear stress is extremely low, meaning that even at this high density the waterways are most probably still safely navigable.

The effect mentioned above is a more local problem in the [PoR](#) as the fluid-mud does not have the same rheological characteristics throughout the port. This is due to the effects of

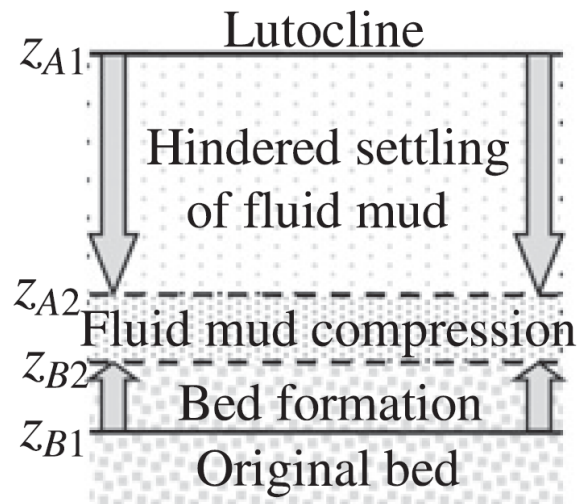


**Figure 1-1:** Fluid-mud settling and bed formation in inactive water [Mehta et al. \(2014\)](#).

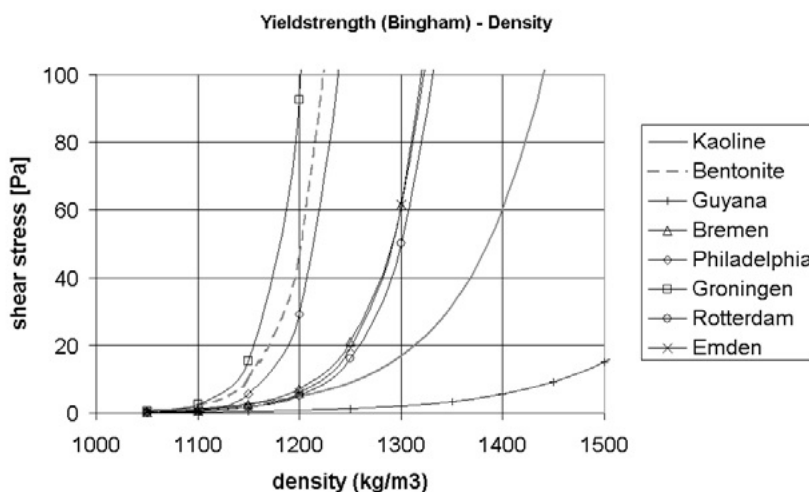


**Figure 1-2:** Relationship of Shear Strength to Mud Density for many ports [Fontein and van der Wal \(2006\)](#).

thixotropy, which is the time and history dependence of the rheological properties of mud. This means that the fluid-mud in a busy channel, that is frequented by many ships, will have different rheological properties than fluid-mud in a channel which is less frequently visited. The fluid-mud in one channel might have completely different rheological characteristics than the fluid-mud in the channel adjacent to it. Therefore, for a new nautical-depth definition to be realistic, a fast and efficient system must be developed for the measurement of the rheological properties of the fluid-mud.

The **PoR** currently use SILAS multi-beam echo-sounders to define where the density of  $1.2 \text{ kgm}^{-3}$  lies at the port bottom. The SILAS system uses calibrated acoustic impedances to determine the location of a certain density level. The water bottom is determined as by the first relevant reflection of the higher frequency (200 to 210  $\text{kHz}$ ) signal. The silt bottom is usually taken as the digitalized signal of the low frequency (24, 33 or 38  $\text{kHz}$ )

signal. The calibration to density consists of a conversion of the acoustic record to a synthetic density profile. The synthetic density profile is then compared to measured density profiles for validation.

Kaya et al. (2008) used ultrasonic echo signals to estimate a soft sea-bottom density profile using ship-mounted equipment. By observing the absorption coefficient of each layer, the acoustic impedance of a layer can be obtained using the received reflection. Wave velocity and density of samples taken from the same sea areas were used to develop a relationship between density and acoustic impedance.

Various techniques exist for measuring the in-situ rheological properties of the fluid-mud, such as Tuning fork measurements, (Fontein and van der Wal (2006)), (Fontein and Byrd (2007)). However, these only provide point measurements and are very inefficient in a port the size of the PoR, especially as the rheological properties can vary within a single harbor channel. Therefore, we need a measurement system that can cover a large area in a relatively short amount of time and can provide in-situ rheological properties of the fluid-mud.

Seismic techniques are obvious techniques to determine the in-situ rheological fluid-mud properties because seismic velocities are directly related to three parameters, namely; density, shear modulus and bulk modulus. Therefore, if relationships between seismic velocities, density and fluid-mud characteristics can be established for fluid-mud from the PoR, rheological properties such as shear modulus could be derived. If the shear modulus and bulk modulus of fluid-mud can be derived from seismic data then, by making a few assumptions, a variety of elastic constants could also be derived. Previous experiments have been undertaken on the PoR fluid-mud by the Flanders Hydraulic Research Institute, (Shahmirzadi et al. (2016)). The parameters investigated include density, peak shear stress and equilibrium flow curves. The results of these experiments will be used for comparison and validation.

However, a fundamental drawback is that shear waves do not propagate through water, meaning that the shear waves in marine streamer data are converted waves and only typically measured with multi-component ocean bottom cables. Using ocean bottom cables is a lengthy and laborious task, complicated by the fact that the properties of the fluid-mud mean that using ocean bottom cables will disturb the fluid-mud making the measurements not in-situ. Furthermore, the cable will also not sit on the water/fluid-mud interface but sink to some level below the interface.

Drijkoningen et al. (2012) showed that under certain conditions marine streamer data contain shear-wave arrivals. This is promising for determining the in-situ rheological properties of the fluid-mud because the source and receivers are not in contact with the fluid-mud and can be towed behind a vessel. This means that a continuous profile can be built of the rheological properties rather than obtaining only point measurements. It also means that the fluid-mud will not be disturbed during measurements and any derived rheological parameters could be representative of the in-situ parameters.

Park et al. (2005) used Multichannel Analysis of Surface Waves (MASW) to characterize the stiffness distribution of water-bottom sediments. The surface wave induced in a water-solid interface is called Scholte wave. However, Park et al. (2005) used a shotgun shell fired into the interface to excite the waves, which would disturb the fluid-mud layer and not provide in-situ measurements. Drijkoningen et al. (2012) used an air gun not in contact with the interface which still resulted in the generation of Schlote waves; such method and waves could

be interesting for the purpose of fluid-mud investigation for the PoR. It could give validation to computed S-wave velocities and define the boundary for the water to fluid-mud interface.

Promisingly, Ha et al. (2010) used a non-invasive acoustic-chirp system to estimate the in-situ bulk density of a clay-water mixture without disturbing the sediment bed.

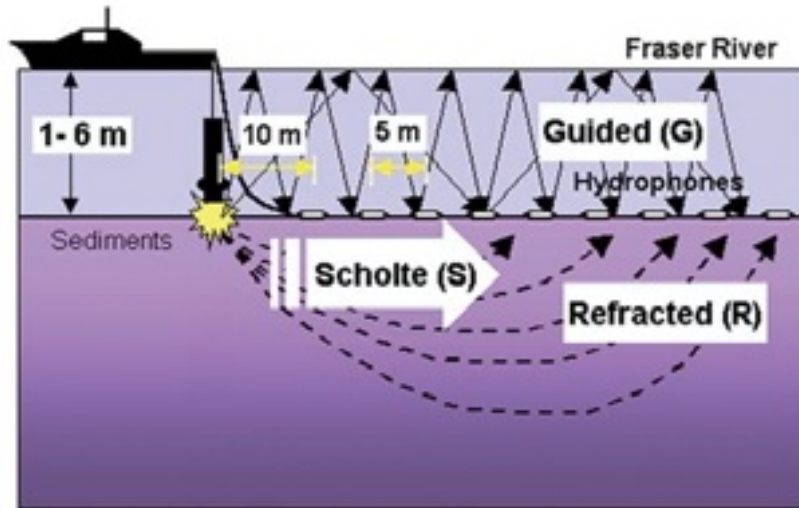


**Figure 1-3:** Schematic of the field setup for the MASW method. Park et al. (2005).

The goals of this MSc thesis are to:

1. Investigate if P-wave and the converted S-wave could be used to determine the in-situ rheological properties of the fluid-mud layer.
2. Investigate if the Scholte wave could be used to determine the in-situ rheological properties of the fluid-mud layer.
3. Investigate how P-wave and S-wave velocity varies with density for the PoR fluid-mud.
4. Investigate how P-wave and S-wave velocity varies with frequency for the PoR fluid-mud.
5. Investigate how P-wave and S-wave velocity varies with time for the PoR fluid-mud.
6. Discuss other methods for determining the in-situ rheological properties of the fluid-mud layer.

**Part II**

**Theory**



---

## Chapter 2

---

# Scholte Wave

### 2-1 Introduction

The Scholte wave is a dispersive interface wave that propagates along a fluid-solid interface. It is similar to a Rayleigh wave (vacuum-solid interface) and a Stoneley wave (solid-solid interface).

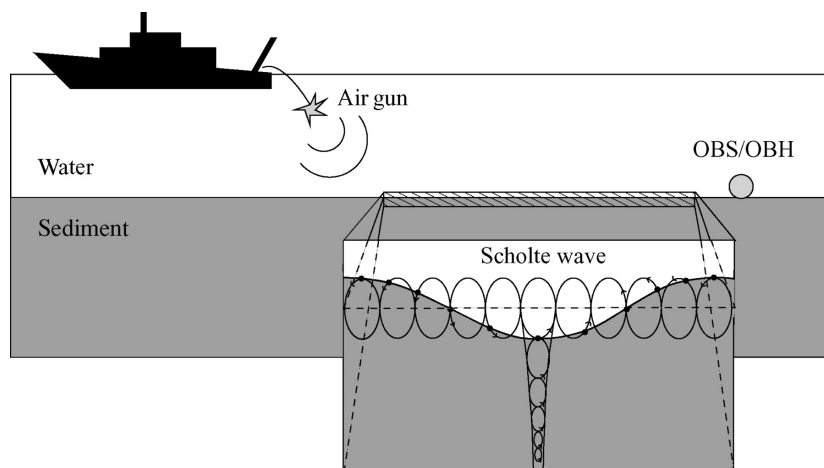


**Figure 2-1:** Excited Scholte Wave at a fluid-solid interface. [Bohlen et al. \(2004\)](#).

### 2-2 Theory - Isotropic Medium

[Scholte \(1958\)](#) will be followed very closely for the theory of the Scholte wave.

In the following, the symbols given below will represent certain parameters.

$A_i$	Constant
$\omega$	Angular frequency
$t$	Time
$x$	x Co-ordinate
$z$	z Co-ordinate
$\theta_i$	Direction (angle with interface)
$c_i$	Velocity
$\mu$	Shear modulus
$K$	Bulk modulus
$\lambda$	Lamé parameter
$\phi_i$	Phase Factor
$\rho$	Density
$\epsilon$	Phase Velocity

**Table 2-1:** Table of Parameters.

Consider two homogeneous isotropic and perfectly elastic semi-infinite half-spaces in contact along a plane  $z = 0$ . A wave in this medium can be expressed as:

$$\exp\left(i\omega\left(t - \frac{(x \sin(\theta_i) \pm z \cos(\theta_i))}{c_i}\right)\right), \quad (2-1)$$

with  $c_i$  being either  $c_1$  and  $c_2$  corresponding to the longitudinal and transverse velocities respectively, given by:

$$c_1 = \sqrt{\frac{(\lambda + 2\mu)}{\rho}}, \quad (2-2)$$

$$c_2 = \sqrt{\frac{\mu}{\rho}}, \quad (2-3)$$

The waves for any given real positive value of  $\frac{\sin(\theta_i)}{c_i}$  can be characterized as:

1. Longitudinal wave ( $c_1$ );
2. Transverse wave ( $c_2$ );
3. Incident wave ( $+\cos(\theta_i)$ );
4. Reflected wave ( $-\cos(\theta_i)$ ).

At the  $z = 0$  boundary the stress disappears for any value of  $x$  and  $t$ , this is only possible for waves with the same values of  $\frac{\sin(\theta_i)}{c_i}$  and  $\omega$ . Rayleigh's requirement is that the amplitude of the surface wave must decrease exponentially with increasing distance along the interface  $z = 0$ . This enforces two conditions on  $\theta_i$ :

1. Because exponential decay with  $z$  is only possible with  $\sin(\theta_i) > 1$ , therefore the phase velocity  $\epsilon = \frac{c_i}{\sin(\theta_i)}$  must be smaller than the velocity  $c_i$ .

2. Two waves that can be initially discarded are those that characterized by a positive imaginary  $\cos(\theta_i)$ , therefore the system only consists of two plane waves.

A longitudinal wave expressed in its exponential form is given by:

$$A_1 \exp\left(i\omega\left(t - \frac{x \sin \theta_1 + z \cos \theta_1}{c_1}\right)\right). \quad (2-4)$$

When travelling in the solid medium, it exerts on the interface  $z = 0$  a stress given by:

$$T_{zx} = \mu\left(\frac{\partial u}{\partial z} + \frac{\partial w}{\partial x}\right) \quad (2-5)$$

and

$$T_{zz} = \lambda\left(\frac{\partial u}{\partial x} + \frac{\partial w}{\partial z}\right) + 2\mu\frac{\partial w}{\partial z}. \quad (2-6)$$

For a longitudinal wave, the vertical and horizontal components of motion are given by:

$$u = A_1 \sin(\theta_1) \cdot \phi_1 \quad (2-7)$$

and

$$w = A_1 \cos(\theta_1) \cdot \phi_1. \quad (2-8)$$

respectively, with  $\phi_1$  being described by:

$$\phi_1 = \exp\left(i\omega\left(t - \frac{x \sin \theta_1 + z \cos \theta_1}{c_1}\right)\right). \quad (2-9)$$

Substituting Equations 2-7 and 2-8 into 2-5 and 2-6, the following expressions are obtained:

$$T_{zx} = -\frac{i\omega A_1 \mu}{c_1} \sin(2\theta_1) \cdot \phi_1, \quad (2-10)$$

$$T_{zz} = -\frac{i\omega A_1}{c_1} (\lambda + 2\mu \cos^2(\theta_1)) \cdot \phi_1, \quad (2-11)$$

with the help of a few trigonometric identities. Hence:

$$\frac{T_{zx}}{T_{zz}} = \frac{\sin(2\theta_1)}{\frac{c_1^2}{c_2^2} - 2\sin^2(\theta_1)}. \quad (2-12)$$

Likewise, for the transverse SV-wave the components of motion are given by:

$$u = A_2 \cos(\theta_2) \cdot \phi_2, \quad (2-13)$$

$$w = -A_2 \sin(\theta_2) \cdot \phi_2 \quad (2-14)$$

with

$$\phi_2 = \exp\left(i\omega\left(t - \frac{x \sin(\theta_2) + z \cos(\theta_2)}{c_2}\right)\right). \quad (2-15)$$

Following the same logic as for the longitudinal wave, the following is obtained for the transverse wave:

$$\frac{T_{zx}}{T_{zz}} = -\cot(2\theta_2). \quad (2-16)$$

A two-wave system is therefore determined by the two following equations:

$$\frac{c_1}{\sin(\theta_1)} = \frac{c_2}{\sin(\theta_2)} = \epsilon \quad (2-17)$$

$$\frac{\sin(2\theta_1)}{\frac{c_1^2}{c_2^2} - 2\sin^2(\theta_1)} = \pm \cot(2\theta_2). \quad (2-18)$$

This expresses the directional equality of the stresses on the interface at  $z = 0$  caused by the incident or reflected longitudinal and transverse waves. Elimination of  $\theta_1$  and  $\theta_2$  using 2-17 leads to the Rayleigh equation for Rayleigh waves:

$$\epsilon^6 c_1^2 - 8\epsilon^4 c_1^2 c_2^2 + 8\epsilon^2 c_2^4 (3c_1^2 - 2c_2^2) - 16c_2^6 (c_1^2 - c_2^2) = 0. \quad (2-19)$$

## 2-3 Theory - Two Isotropic Half-spaces

We now extend the theory to a system in which two homogeneous isotropic and perfectly elastic half-spaces are in contact along a plane  $z = 0$ . Consider that the top halfspace is a liquid medium with shear stress/ rigidity that is zero:  $\mu = 0$ .

Similar to Section 2-2, the stress exerted on the interface by a longitudinal wave is given by:

$$T_{zx} = -i\omega\rho c_1 A_1 \cdot 2\sin^2(\theta_2) \cot(\theta_1) \quad (2-20)$$

$$T_{zz} = -i\omega\rho c_1 A_1 \cdot \cos(2\theta_2) \quad (2-21)$$

which are derived from Section 2-2 by introducing  $\theta_2$ , the phase factor has been omitted:

$$\sin(\theta_2) = \frac{c_2}{c_1} \sin(\theta_1). \quad (2-22)$$

In a liquid medium, a wave can be expressed by:

$$A'_1 \exp\left(i\omega\left(t - \frac{x \sin(\theta'_1) + z \cos(\theta'_1)}{c'}\right)\right) \quad (2-23)$$

with prime denoting fluid properties. Following the condition that the vertical motion must be continuous in both the solid and liquid medium,

$$\frac{\sin(\theta'_1)}{c'_1} = \frac{\sin(\theta_1)}{c_1} \quad (2-24)$$

and

$$A'_1 \cos(\theta'_1) = A_1 \cos(\theta_1). \quad (2-25)$$

This wave exerts a vertical stress on the interface equal to:

$$T_{zz} = -i\omega\rho' c'_1 A'_1 = -i\omega\rho' c_1 A_1 \cdot \frac{\cot(\theta_1)}{\cot(\theta'_1)}. \quad (2-26)$$

The result is a stress difference at the interface given by:

$$\Delta T_{zx} = -i\omega\rho c_1 A_1 2 \sin^2(\theta_2) \cot(\theta_1) \quad (2-27)$$

$$\Delta T_{zz} = -i\omega\rho c_1 A_1 2 \left( \cos(2\theta_2) - \frac{\rho' \cot(\theta_1)}{\rho \cot(\theta_1')} \right). \quad (2-28)$$

Consequently,

$$\left( \frac{\Delta T_{zx}}{\Delta T_{zz}} \right)_L = \frac{2 \sin^2(\theta_2) \cot(\theta_1)}{\cos(2\theta_2) - \frac{\rho' \cot(\theta_1)}{\rho \cot(\theta_1')}} \quad (2-29)$$

with L denoting this is for a longitudinal wave. Following the same methodology in the case of a transverse wave, the wave can be expressed by:

$$A_2 \exp \left( i\omega \left( t - \frac{x \sin(\theta_2) + z \cos(\theta_2)}{c_2} \right) \right) \quad (2-30)$$

with ( $\phi_2$  being omitted)

$$T_{zx} = -i\omega\rho c_2 A_2 \cos(2\theta_2) \quad (2-31)$$

$$T_{zz} = +i\omega\rho c_2 A_2 2 \sin^2(\theta_2) \cot(\theta_2). \quad (2-32)$$

The accompanying wave in the liquid is propagating in the  $\theta_1'$  direction given by:

$$\frac{\sin(\theta_1')}{\sin(\theta_2)} = \frac{c_1'}{c_2} \quad (2-33)$$

with an amplitude  $A_1'$  which satisfies

$$A_1' \cos(\theta_1') = -A_2 \sin(\theta_2). \quad (2-34)$$

Using Equations 2-33 and 2-34 to eliminate  $C_1'$  and  $A_1'$ , respectively, in Equation 2-26, leads to:

$$T_{zz} = i\omega\rho' A_2 c_2 \frac{1}{\cot(\theta_1')}, \quad (2-35)$$

which describes the stress exerted by the transverse wave in the fluid. Therefore, the stress differences are:

$$\Delta T_{zx} = -i\omega\rho c_2 A_2 \cos(2\theta_2) \quad (2-36)$$

$$\Delta T_{zz} = i\omega\rho c_2 A_2 \left( 2 \sin^2(\theta_2) \cot(\theta_2) - \frac{\rho'}{\rho \cot(\theta_2)} \right). \quad (2-37)$$

Consequently,

$$\left( \frac{\Delta T_{zx}}{\Delta T_{zz}} \right)_T = -\frac{\cos(2\theta_2)}{2 \sin^2(\theta_2) \cot(\theta_2) - \frac{\rho'}{\rho \cot(\theta_2)}}, \quad (2-38)$$

with T denoting that this is for a transverse wave. The stress on the interface must be continuous, which means the stress-differences have to disappear, which is only possible when

$\left( \frac{\Delta T_{zx}}{\Delta T_{zz}} \right)_L = \left( \frac{\Delta T_{zx}}{\Delta T_{zz}} \right)_T$ . This leads to the following equation:

$$\frac{2 \sin^2(\theta_2) \cot(\theta_1)}{\cos(2\theta_2) - \frac{\rho' \cot(\theta_1)}{\rho \cot(\theta_1')}} = -\frac{\cos(2\theta_2)}{2 \sin^2(\theta_2) \cot(\theta_2) - \frac{\rho'}{\rho \cot(\theta_2)}} \quad (2-39)$$

or, upon simplifying

$$\cos^2(2\theta) + 4 \sin^4(\theta_2) \cot(\theta_1) \cot(\theta_2) - \frac{\rho' \cot(\theta_1)}{\rho \cot(\theta_1')} = 0. \quad (2-40)$$

To find when the Scholte wave exists, the above equation can be displayed in terms of wave velocity and phase velocity. In the case  $\cot(\theta_1)$  and  $\cot(\theta_2)$  are positive imaginary and  $\cot(\theta_1')$  negative imaginary, by using the definition

$$\epsilon = \frac{c_2}{\sin(\theta_2)}, \quad (2-41)$$

the following equation is obtained:

$$(2c_2^2 - \epsilon^2)^2 - 4 \frac{c_2^3}{c_1} \sqrt{(c_2^2 - \epsilon^2)(c_1^2 - \epsilon^2)} + \frac{\rho' c_1'}{\rho c_1} \epsilon^4 \sqrt{\frac{(c_1^2 - \epsilon^2)}{(c_1'^2 - \epsilon^2)}} = 0 \quad (2-42)$$

with  $\epsilon^2 < c_i^2$ . It is obvious a root exists for every value of the material constant.

For small values of the ratio between the acoustic impedance in the liquid ( $\rho' c_1'$ ) and solid ( $\rho c_1$ ), the transfer of energy of the waves from the solid to the liquid medium will also be small. Therefore, the wave propagation in the solid body will only be slightly influenced by the liquid, meaning the velocity of the Scholte-wave will be approximately the velocity of a Rayleigh wave for a solid - vacuum interface. This is evident if we apply the condition that  $\frac{\rho_1' c_1'}{\rho c_1} \ll 1$  to Equation 2-42:

$$(2c_2^2 - \epsilon^2)^2 - 4 \frac{c_2^3}{c_1} \sqrt{(c_2^2 - \epsilon^2)(c_1^2 - \epsilon^2)} = 0. \quad (2-43)$$

In the case where  $c_1'$  is much smaller than  $c_2$ , the velocity of the Scholte wave is also much smaller than  $c_2$ . For this case, if  $\epsilon = c_R$  the third term of Equation 2-42 becomes imaginary with the real part of the root being approximately equal to  $c_R$ . This wave system closely resembles the Rayleigh wave for a solid-vacuum setup but the imaginary part of the root gives rise to an exponential decrease in the horizontal direction.

## 2-4 Use for parameter determination

Because the Scholte wave is a linear event, the slowness, and therefore velocity, should be easily determined from a seismic section. The S-wave velocity can therefore be calculated by using the formula for Scholte-wave velocity propagating along the interface between a fluid half-space and an isotropic elastic half-space given by Vinh (2013). First the following parameter ratios were defined:

$$\chi = \frac{c_{sch}^2}{c_2^2} \quad (2-44)$$

$$\gamma = \frac{c_2^2}{c_1^2} \quad (2-45)$$

$$\gamma_f = \frac{c_2^2}{c_f^2} \quad (2-46)$$

$$r = \frac{\rho_f}{\rho}, \quad (2-47)$$

where  $c_{sch}$ ,  $c_f$  and  $\rho_f$  are the Scholte-wave velocity, P-wave velocity of the fluid and density of the fluid, respectively.  $\chi$  is also known as the dimensionless velocity. For the regime  $0 < \gamma_f < \gamma < 1$  which is the same as  $c_f > c_1 > c_2$  the dimensionless velocity can be written as:

$$\chi_{sc} = -\frac{A_2}{A_3} - \frac{1}{\gamma} - I_0 \quad (2-48)$$

with:

$$A_2 = 4\sqrt{\gamma\gamma_f} - \frac{r}{2}\left(\sqrt{\gamma} + \frac{1}{\sqrt{\gamma}}\right) - \frac{1}{2}\left(9\sqrt{\gamma_f} + \frac{1}{\sqrt{\gamma}}\right), \quad (2-49)$$

$$A_3 = r\sqrt{\gamma} + \sqrt{\gamma_f}, \quad (2-50)$$

$$I_0 = \frac{1}{\pi} \left( - \int_1^{\frac{1}{\gamma}} \arctan(\phi_1(t)) dt + \int_{\frac{1}{\gamma}}^{\frac{1}{\gamma_f}} \arctan(\phi_2(t)) dt \right), \quad (2-51)$$

$$\phi_1(t) = \frac{rt^2\sqrt{1-\gamma t} + (t-2)^2\sqrt{1-\gamma_f t}}{4\sqrt{t-1}\sqrt{1-\gamma t}\sqrt{1-\gamma_f t}} \quad (2-52)$$

and

$$\phi_2(t) = \frac{\sqrt{1-\gamma_f t} \left[ (t-2)^2 + 4\sqrt{t-1}\sqrt{\gamma t-1} \right]}{rt^2\sqrt{\gamma t-1}}. \quad (2-53)$$

Like-wise, for the regime  $0 < \gamma < \gamma_f < 1$  or  $c_1 > c_f > c_2$ :

$$\chi_{sc} = -\frac{A_2}{A_3} - \frac{1}{\gamma_f} - I_0, \quad (2-54)$$

where  $A_2$ ,  $A_3$  and  $\phi_1(t)$  are calculated by Equations 2-49, 2-50 and 2-52 respectively while.

$$I_0 = \frac{1}{\pi} \left( - \int_1^{\frac{1}{\gamma_f}} \arctan(\phi_1(t)) dt + \int_{\frac{1}{\gamma_f}}^{\frac{1}{\gamma}} \arctan(\phi_2(t)) dt \right) \quad (2-55)$$

and

$$\phi_2(t) = \frac{\sqrt{1-\gamma t} \left[ (rt^2 + 4\sqrt{t-1}\sqrt{\gamma_f t-1}) \right]}{(2-t)^2\sqrt{\gamma_f t-1}}. \quad (2-56)$$

Finally, for the regime  $0 < \gamma < 1 < \gamma_f$  or  $c_1 > c_2 > c_f$ :

$$\chi_{sc} = -\frac{A_2}{A_3} - \frac{1}{2} \left( 1 + \frac{1}{\gamma_f} \right) - I_0 \quad (2-57)$$

with

$$A_2 = -\frac{1}{2} \left( \sqrt{\frac{\gamma}{\gamma_f}} + \sqrt{\frac{\gamma_f}{\gamma}} \right) - 4\gamma_f - 1 + 4\gamma_f\sqrt{\gamma}, \quad (2-58)$$

$$A_3 = r \sqrt{\gamma \gamma_f} + \gamma_f, \quad (2-59)$$

$$I_0 = \frac{1}{\pi} \left( - \int_{\frac{1}{\gamma_f}}^1 \arctan(\phi_1(t)) dt + \int_1^{\frac{1}{\gamma}} \arctan(\phi_2(t)) dt \right), \quad (2-60)$$

$$\phi_1(t) = \frac{\sqrt{\gamma_f t - 1} \left[ (t - 2)^2 - 4\sqrt{1 - t}\sqrt{1 - \gamma t} \right]}{rt^2 \sqrt{1 - \gamma t}} \quad (2-61)$$

and

$$\phi_2(t) = \frac{\sqrt{1 - \gamma t} \left[ rt^2 + 4\sqrt{t - 1}\sqrt{\gamma_f t - 1} \right]}{(t - 2)^2 \sqrt{\gamma_f t - 1}}. \quad (2-62)$$

Using these three regimes, the Scholte-wave velocity is plotted for varying S-wave velocities and densities (Figure 2-2). The P-wave velocity of the water and solid are chosen to be  $1500 \text{ m.s}^{-3}$  and  $1600 \text{ m.s}^{-1}$ , respectively and with the density of the fluid taken as water at  $1000 \text{ kg.m}^{-3}$ . The fluid mud is expected to have a density ranging from  $1100$  to  $1250 \text{ kg.m}^{-3}$  (Shahmirzadi et al. (2016)).

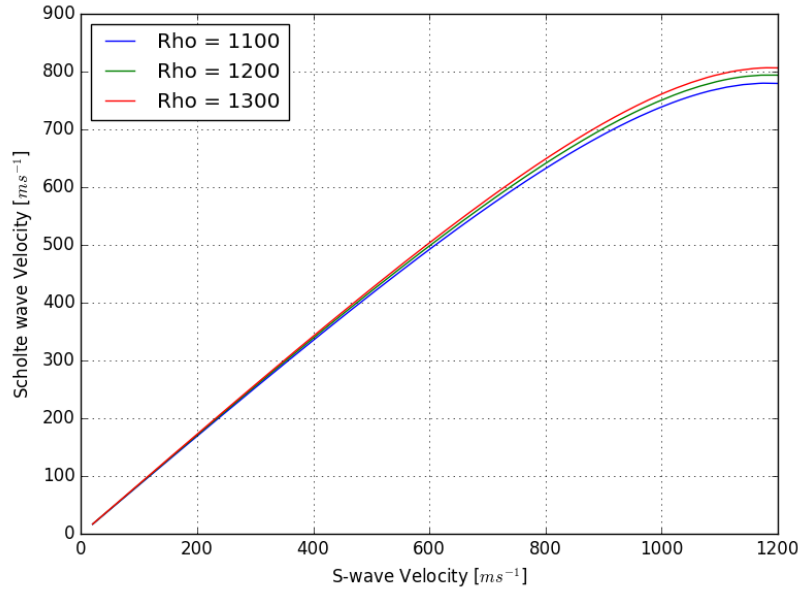


**Figure 2-2:** How the Scholte wave velocity varies with S-wave velocity and density.

The first observation of the plotted data is that the Scholte-wave velocity does not significantly vary with density at S-wave velocities below  $1000 \text{ m.s}^{-1}$ . The second observation is that also below S-wave velocities of  $800 \text{ m.s}^{-1}$  the relationship between the Scholte-wave velocity and S-wave velocity is nearly linear. The fluid mud is expected to have low S-wave velocities and a density between  $1000 \text{ kg.m}^{-3}$  and  $1300 \text{ kg.m}^{-3}$ , which would fall into this linear relationship.

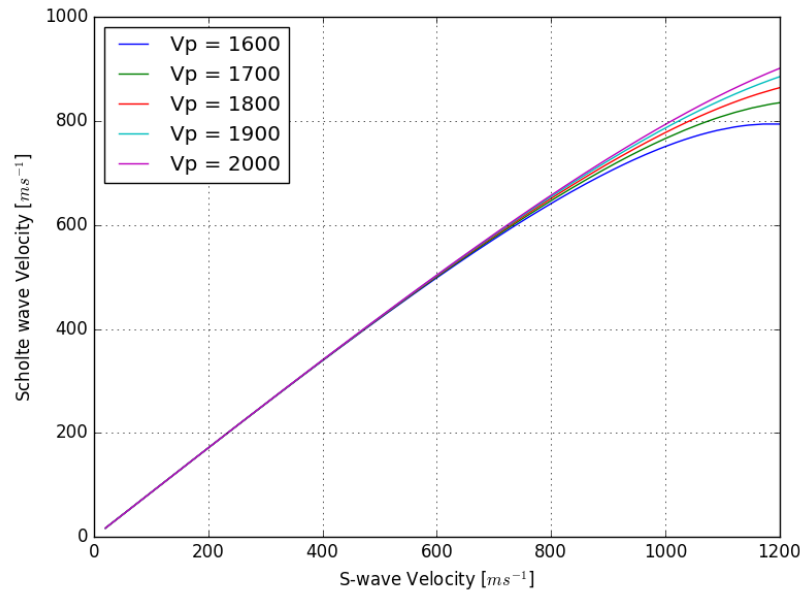


**Figure 2-3:** How the Scholte wave velocity varies with S-wave velocity and P-Wave velocity.

The Scholte-wave velocities were also plotted for a varying P-wave velocity (fluid-mud density being  $1200 \text{ kg.m}^{-3}$ ) and is shown in Figure 2-3. Promisingly, again below S-wave velocities of  $1000 \text{ m.s}^{-1}$  there is hardly any variation in the Scholte-wave velocity. This could provide the foundation for a quick S-wave velocity determination and hence shear modulus of the surface of the fluid mud.

### 2-4-1 Shear Modulus

By using the simple relationship of S-wave velocity to shear modulus given in Equation 2-3, a graph of the Scholte-wave and its corresponding S-wave velocity and shear modulus is shown in Figure 2-4. If the Scholte-wave velocity and density of the fluid-mud is known, then the S-wave velocity and the shear modulus can be estimated from the corresponding plot.

### 2-4-2 Bulk Modulus

Using the definitions for P-wave and S-wave velocities from Equations 2-2 and 2-3, respectively, the bulk modulus can be determined. By using the identity for the Lamé parameter ( $\lambda = K - \frac{2\mu}{3}$ ), both are rearranged for density and set equal to each other to yield:

$$\frac{K + \frac{4}{3}\mu}{v_p^2} = \frac{\mu}{v_s^2} \quad (2-63)$$

Rearranging in the form of  $y = mx + c$  gives:

$$\frac{v_p^2}{v_s^2} = K \frac{1}{\mu} + \frac{4}{3} \quad (2-64)$$

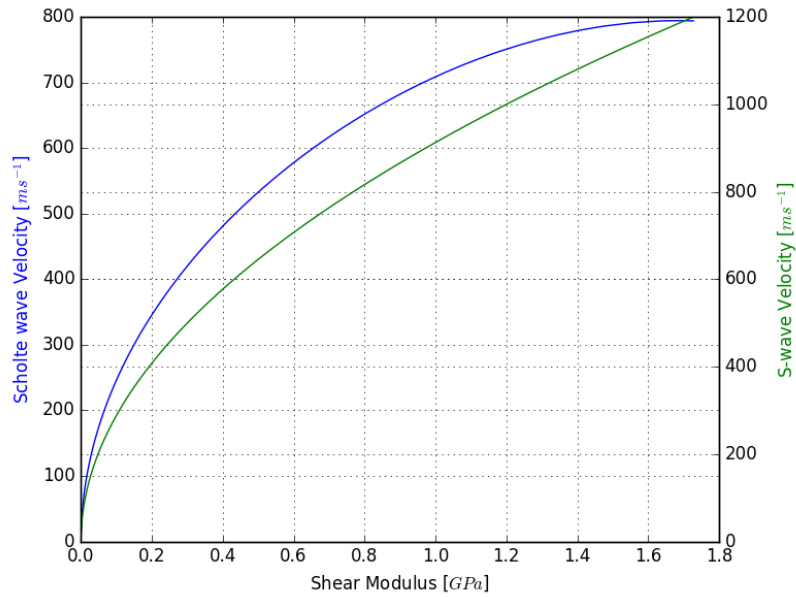


**Figure 2-4:** How the shear modulus varies with a change in Scholte wave (blue) and S-wave velocity (green) for a fluid-mud density of  $1200 \text{ kg.m}^3$ .

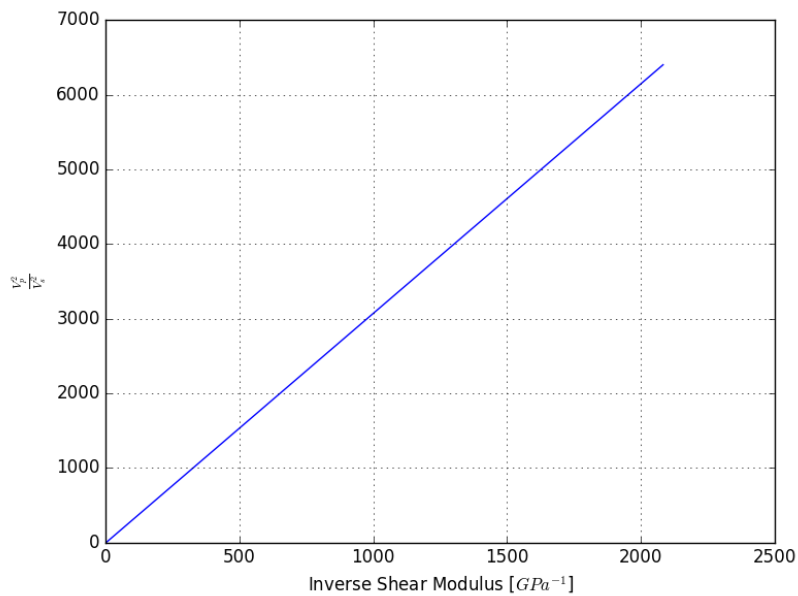


**Figure 2-5:** Squared velocity ratio against the inverse shear modulus for a density of the fluid-mud of  $1200 \text{ kgm}^{-3}$ . The gradient of the plot is equal to the bulk modulus.

Therefore, if the squared ratio of P to S-wave velocity and the shear modulus are known, the bulk modulus can be determined by the gradient of the plot or by simply rearranging Equation 2-64 for the bulk modulus.

### 2-4-3 Elastic Constants

Hamilton (1971) concluded that for small stresses, water-saturated sediments respond elastically and that the elastic equations of the Hookean model can be used to compute unmeasured elastic constants. If we treat the fluid-mud as an isotropic, linear elastic and highly saturated marine sediment, then a variety of elastic constants can be derived by knowing the shear and bulk modulus. By using the following Hookean equations defined by Birch (1961) many other elastic parameters can be obtained (Table 2-2).

Young's modulus (E)	Lamé's Constant ( $\lambda$ )	Poisson's Ratio ( $\nu$ )	P-wave Modulus (M)
$\frac{9K\mu}{3K+\mu}$	$K - \frac{2\mu}{3}$	$\frac{3K-2\mu}{6K+2\mu}$	$K + \frac{4\mu}{3}$

**Table 2-2:** A table of elastic constants derived from the Bulk and Shear modulus for a isotropic, linear elastic medium.



**Part III**

**Modelling**



---

## Chapter 3

---

# Modelling

The aims of modelling the fluid-mud system are to:

1. Investigate if reflected S-waves can be detected in the water, fluid-mud and solid configuration.
2. Investigate if the Scholte wave can be identified and velocity derived.
3. Investigate the effect of source and receiver height in the detection of such waves.

An elastic finite-difference wave-field modelling software (Thorbecke and Draganov (2011)) was used to model the fluid-mud system. The model consists of 3 layers, which are a water layer, a fluid-mud layer and a solid medium. The P-wave velocity, S-wave velocity and density profiles are described in Figure 3-1. The dimensions of the model were 100m  $\times$  210m, the size was chosen to limit multiples from the physical boundaries of the model.

### 3-1 The Effects of Source and Receiver Height above the Fluid-Mud

The model will be run with varying heights of the source and receivers above the fluid-mud, to see what effect the height has on detection. The heights used are: 10 m, 5 m, 2 m, 1 m, 0.5 m and 0.2 m. The corresponding raw shot records are shown in Figures 3-2 - 3-7.

The heights of 0.2 m, 0.5 m and 1 m clearly show the Scholte wave and the PS reflection from the fluid-mud solid interface. The reflection hyperbola starts at approximately 0.2 ms. This is further backed up by calculations of expected arrival times of the PS-wave and by its obvious slow velocity compared to other events. With the height of 2 m, the PS-wave is very faint, while there is no evidence of the Scholte wave. For the source and receiver height of 10 m and 5 m, the model only shows P-Wave reflections and multiples.

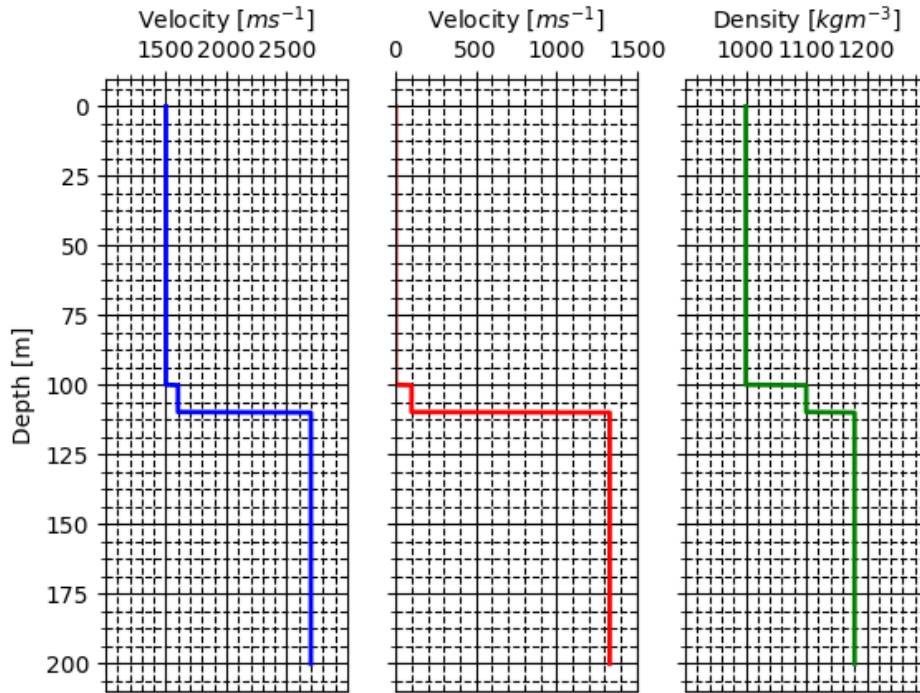


**Figure 3-1:** The model parameters used in the 3 layer model. P-wave velocity (Blue), S-wave velocity (Red) and Density (Green).

### 3-2 Velocity Determination

For the determination of the Scholte-wave velocity an height of 1 m was used. Measuring the velocity from the inverse of the Scholte-wave gradient gives a velocity of  $86 \text{ m}\cdot\text{s}^{-1}$ .

The P-wave velocity of the fluid-mud can be determined also by the application of an NMO to the modelled data. In doing so, the hyperbolic first P-wave arrival becomes linear at a velocity of  $1600 \text{ m}\cdot\text{s}^{-1}$

For S-wave-velocity determination, the density also needs to be determined. This is achieved by measuring the amplitude of the incident and reflected P-wave, in doing so the reflection coefficient ( $R$ ) can be determined for the water-fluid-mud interface (Equation 3-1). The density can be directly calculated because the density and P-wave velocity of water is known:

$$R = \frac{\rho_2 c_2 - \rho_1 c_1}{\rho_2 c_2 + \rho_1 c_1}. \quad (3-1)$$

Using the measured Scholte wave, P-wave velocity and calculated density, the S-wave velocity can be determined. By using Figure 3-8 the S-wave velocity is calculated to be  $100 \text{ m}\cdot\text{s}^{-1}$ .

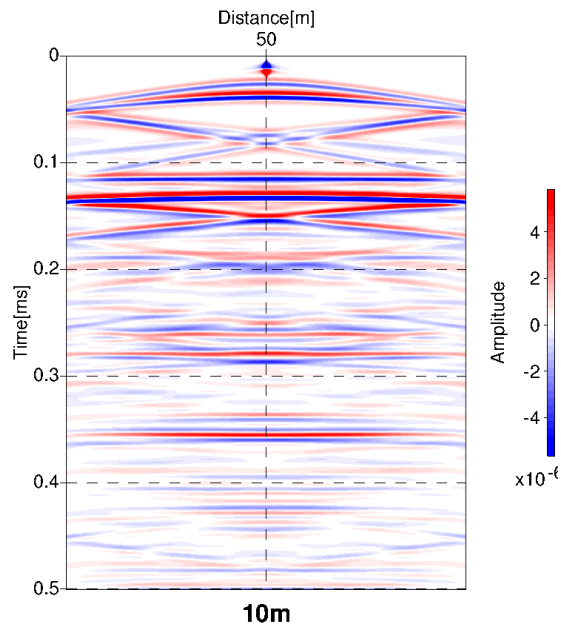


Figure 3-2: Modelled seismic response with an offset of 10 m .

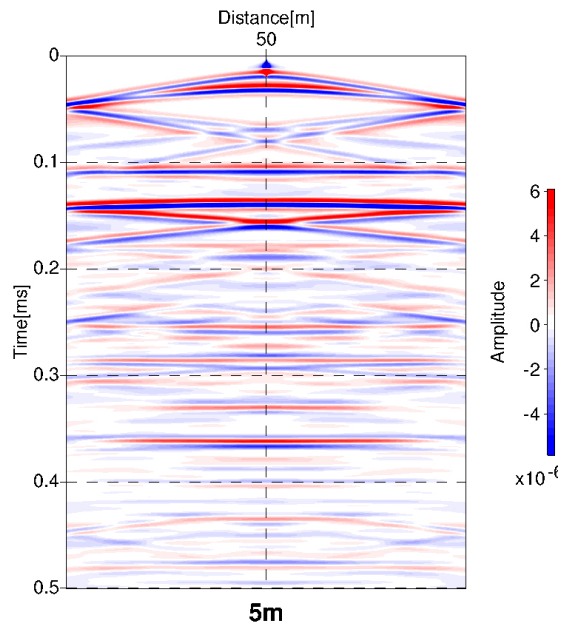
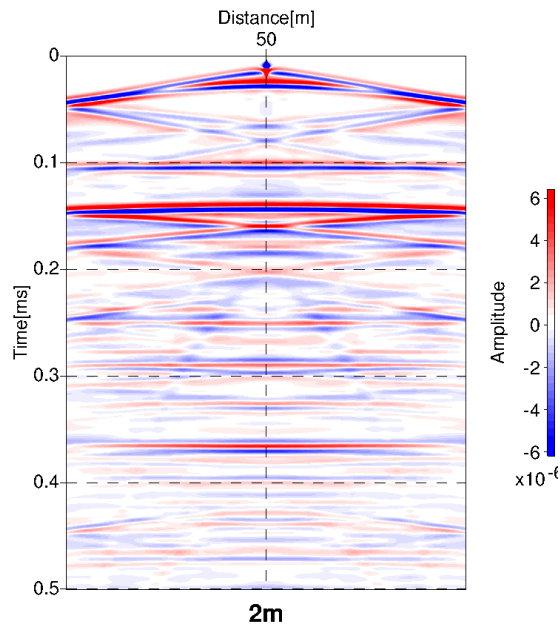
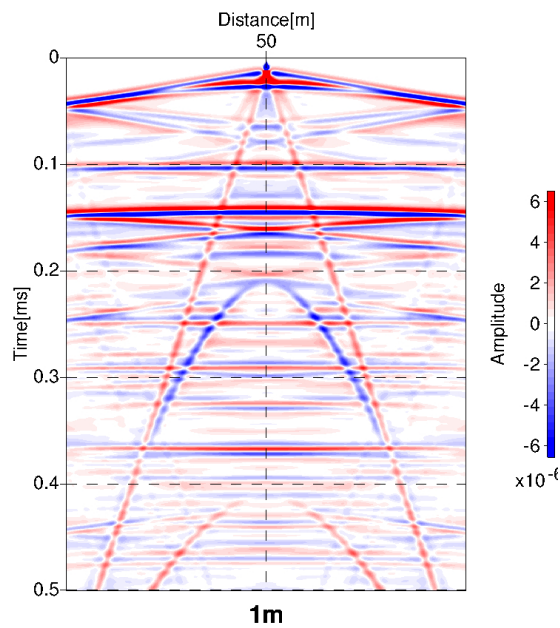


Figure 3-3: Modelled seismic response with an offset of 5 m .



**Figure 3-4:** Modelled seismic response with an offset of 2 m .



**Figure 3-5:** Modelled seismic response with an offset of 1 m .

### 3-3 Shear and Bulk Modulus

By knowing the Scholte-wave velocity and S-wave velocity, the shear modulus can be derived. By using Figure 3-8, the shear modulus is calculated to be 12 MPa. Now by knowing the

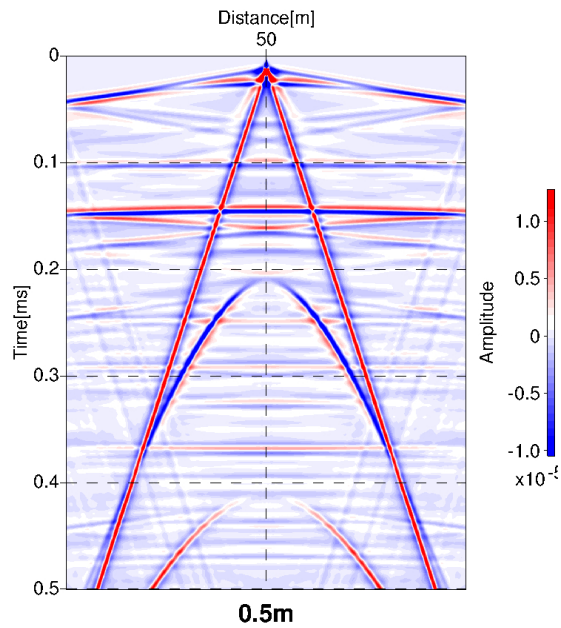


Figure 3-6: Modelled seismic response with an offset of 0.5 m .

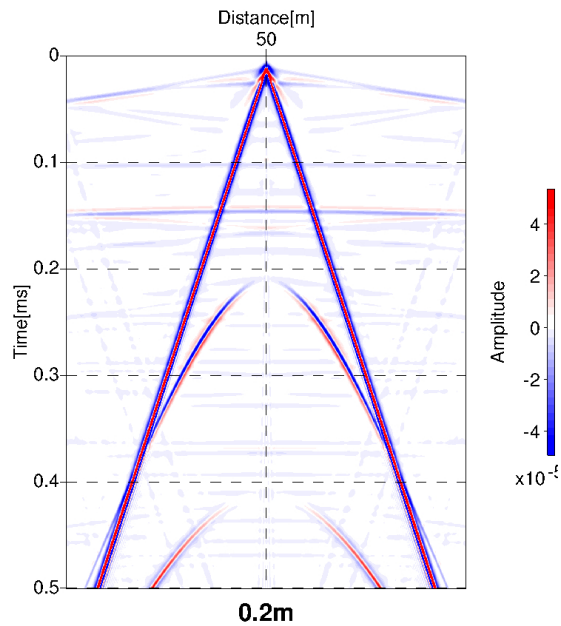
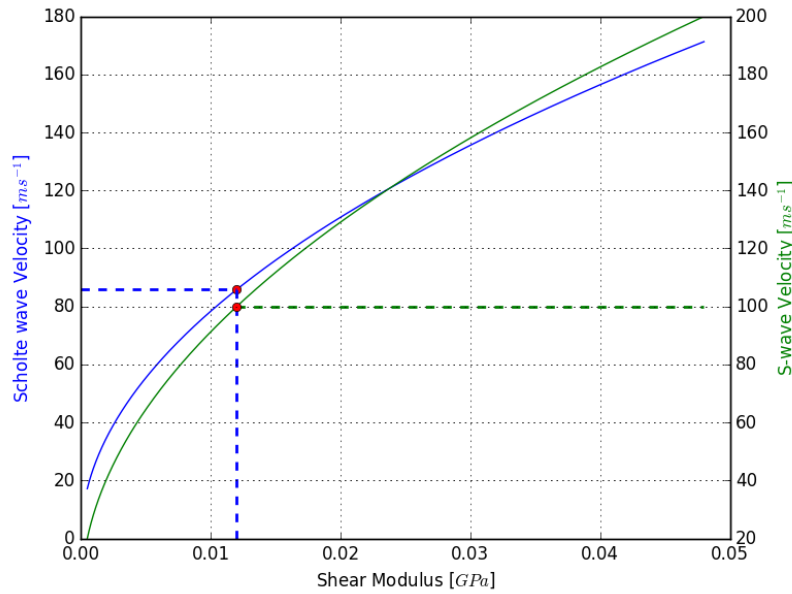


Figure 3-7: Modelled seismic response with an offset of 0.2 m .

shear modulus, P-wave and S-wave velocity, Equation 2-64 can be solved for the bulk modulus. By using the previously derived values, a Bulk modulus of 3.07 *GPa* is calculated.



**Figure 3-8:** How the shear modulus varies for low Scholte-wave (blue) and S-wave (green) velocities for a fluid-mud density of  $1200 \text{ kg.m}^{-3}$ .

### 3-4 Elastic Parameters

Using the derived shear modulus and bulk modulus, the following elastic parameters are calculated using the equations in Table 3-1:

Young's modulus (E)	Lamé's Constant ( $\lambda$ )	Poisson's Ratio ( $\nu$ )	P-wave Modulus (M)
0.36 GPa	3.06 GPa	0.498	3.09 GPa

**Table 3-1:** A table of elastic constants from the modelled data.

If the density, P-wave and S-wave velocity can be determined for the solid layer that lies under the fluid-mud layer, the elastic constants can be interpolated for the thickness of the fluid-mud. Assuming that the characteristics of the solid layer are known, four models of how the density and therefore shear strength varies with depth are considered. These are: a linear behaviour [Kaya et al. \(2008\)](#), exponential behaviour, an average of the two (denoted as mid-line) and a tanh function [Jia et al. \(2013\)](#), [Hwang et al. \(1989\)](#). An arbitrary thickness of 2 m is chosen for the fluid-mud layer for demonstration purposes.

The linear density behaviour represents a system which includes compaction but neglects thixotropy, therefore the density of the particles at the bottom of the fluid-mud is only effected by the fluid-mud above it. The exponential density behaviour represents a system which includes the compaction and thixotropy, therefore not only is the density at the bottom effected by the fluid-mud above (compaction), but it also includes the time-dependent

property of 'shear thinning'. The exponential model is expected to represent the density profile of fluid-mud for infinite settlement time. The density behaviour of fluid-mud will most likely vary somewhere in between linear and exponential, which is described by the mid-line. The tanh function is also considered because density profiles have been measured in previous studies and resemble a tanh function. It is predicted to represent fluid-mud with some consolidation and thixotropy effects.

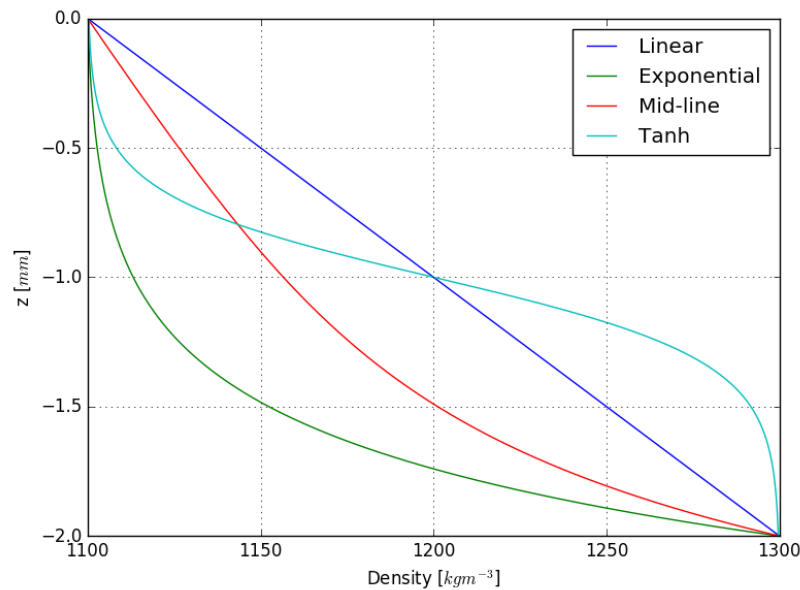


**Figure 3-9:** The four models of how the density varies with depth for fluid-mud.

The Flanders Hydraulics Research Center undertook density measurements of how density varies with height and time for fluid-mud from the PoR, [Shahmirzadi et al. \(2016\)](#). The following remarks were made:

1. Density of the top sub-samples is significantly lower than that of deeper sub samples.
2. The density distribution along the depth of column showed a general increase with time.

The report shows that that at day 1 the density of the fluid-mud has a linear behaviour of density with height. After 56 days, the density varies with behaviour similar to the mid-line with height. The top of the fluid-mud was just above  $1100 \text{ kg.m}^{-3}$  and at the bottom it had a density of approximately  $1200 \text{ kg.m}^{-3}$ .

Concerning the shear modulus, one would expect that an increase in density would cause an increase in the shear modulus, due to increased friction between particles and considering that as fluid-mud increases in density it would become less 'fluid-like' and more 'mud-like'. Therefore it would be novel to use the same model for density as shear modulus. The linear, exponential, mid line and tanh model is shown in Figure 3-10.

The first positive observation from the plot is that the linear model and mid-line model are representative of the measurements in the report from [Shahmirzadi et al. \(2016\)](#) for shear

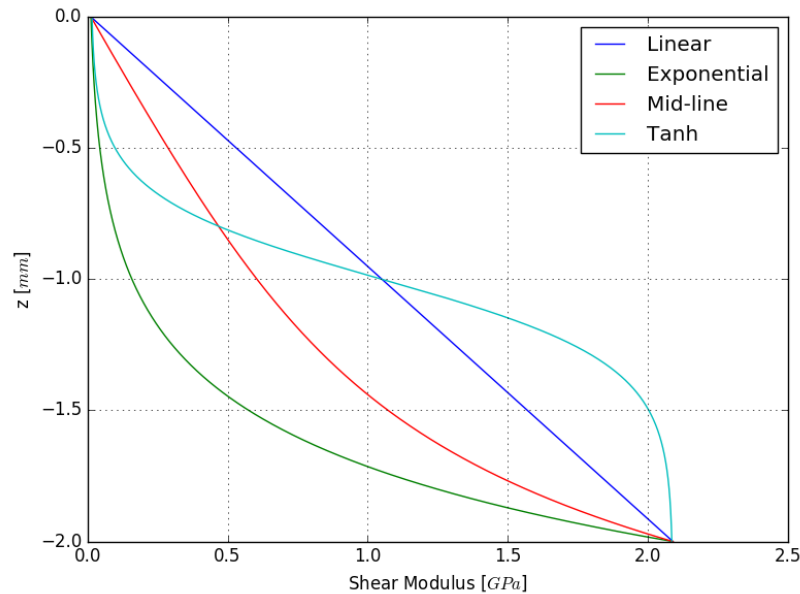


**Figure 3-10:** The four models of how the shear modulus varies with depth for fluid-mud.

stress. The mid-line model describes the measured height against shear stress relationship well for day 56 and the linear relationship matches day 1 well. However, the increase of the shear stress over time at the bottom and top of the fluid-mud layer has not been taken into account in the case presented in this report. Both these values are fixed in the models presented.

Promisingly, when the plot of shear modulus against density is created, two of the models, again, describe the same relationship as [Shahmirzadi et al. \(2016\)](#), with the day 1 measurements being described by the linear model and day 56 being described by the mid-line model.

With models describing the density and shear modulus, a model for the S-wave velocity can be determined. The four models are shown in [Figure 3-12](#). If the results are directly interpreted from the density and shear modulus data, then the linear relationship should represent the S-wave velocity profile of day 1. Likewise, the mid-line should represent the S-wave velocity of day 56.

Assuming the P-wave velocity also has a linear, exponential, mid-line and tanh relationship between the measured P-wave velocity at the water - fluid-mud interface and the fluid-mud - solid interface and using [Equation 2-64](#), the bulk modulus can be determined. The four different models for bulk modulus are shown in [Figure 3-13](#). The linear bulk modulus first decreases and then increases with depth, which, if the comparison with [Shahmirzadi et al. \(2016\)](#) is correct then this is the representation of the bulk modulus for day 1 of the fluid-mud deposition. The exponential model first greatly increases until approximately  $\frac{7}{10}$  of the total depth. The bulk modulus then sharply decreases for the remaining depth. The mid-line between the linear and exponential has a gradual increase in bulk modulus to  $\frac{7}{10}$  of the total depth. It then has a sharp decrease for the remaining depth. Again this could be representative of day 56 of the fluid-mud settlement.

Knowing the bulk and shear modulus allows for the determination of the elastic constants

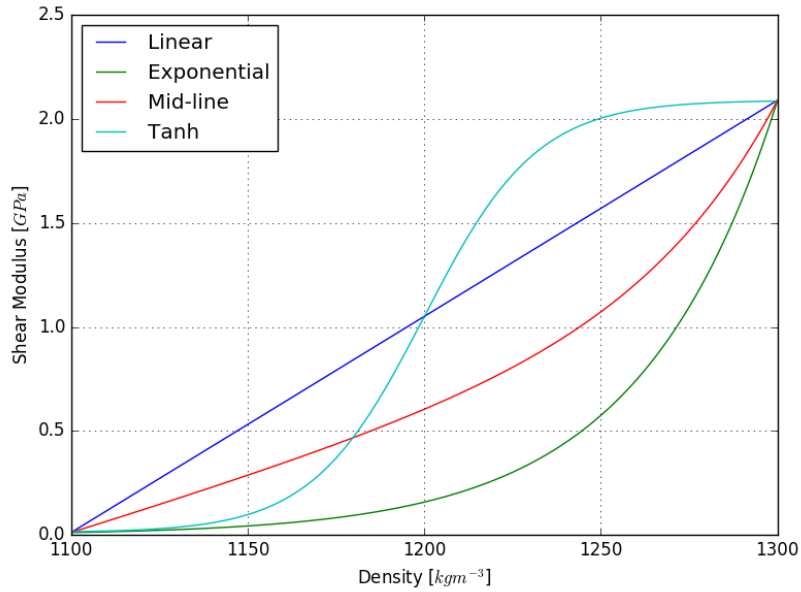


**Figure 3-11:** The three models of how the Shear modulus varies with density for fluid-mud.

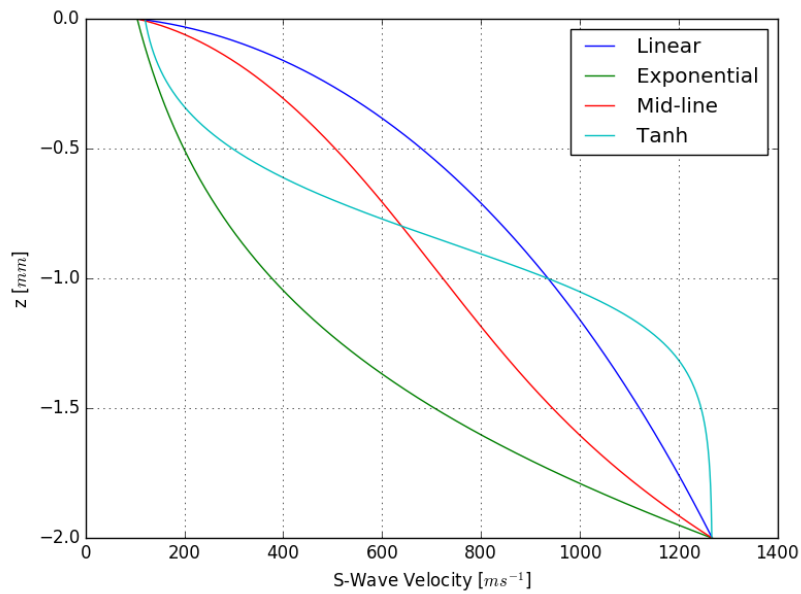
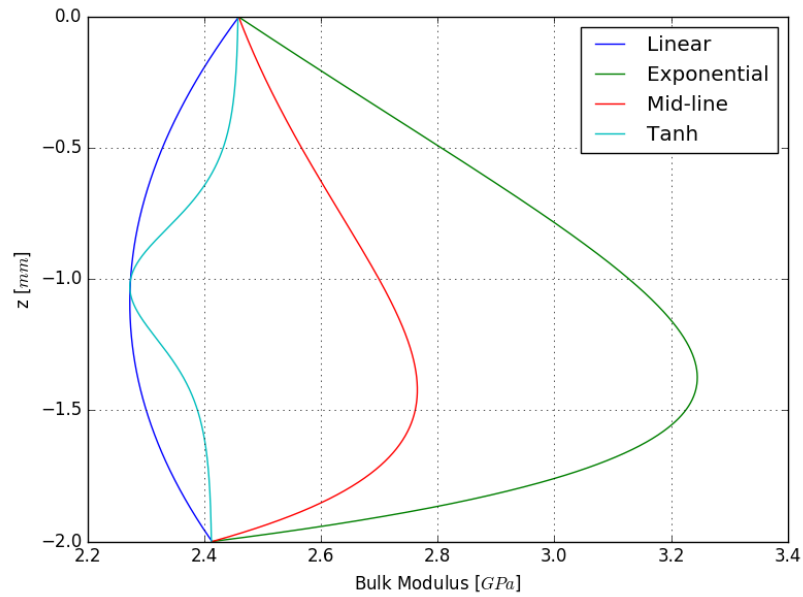


**Figure 3-12:** The three models of how the S-wave velocity varies with depth for fluid-mud.

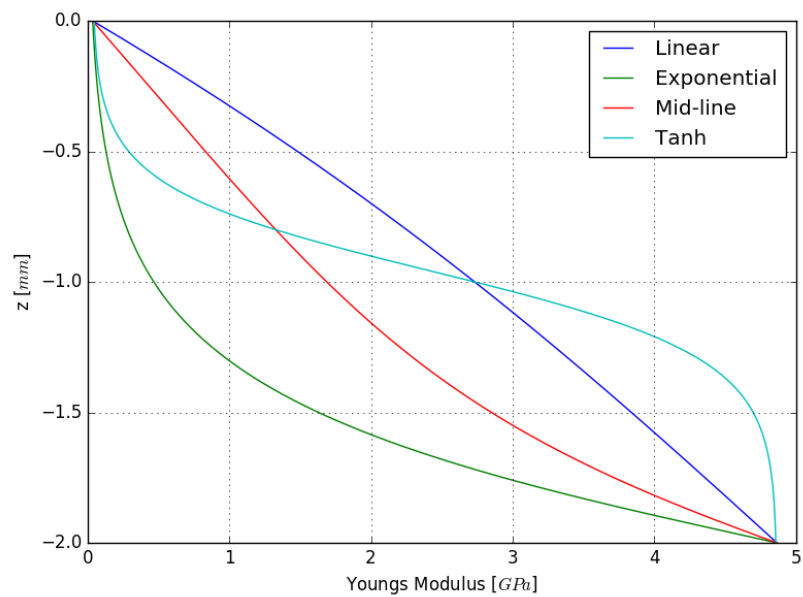
by using the equations given in Table 2-2. Graphics of how these elastic constants vary with depth are shown below.

Figure 3-14 displays how the Young’s modulus varies with depth for fluid-mud. All models describe an increase in Young’s modulus as depth increases. This means that the stiffness of the fluid-mud is increasing with depth for these models.

Figure 3-15 displays how the first Lamé parameter is expected to behave with depth for the



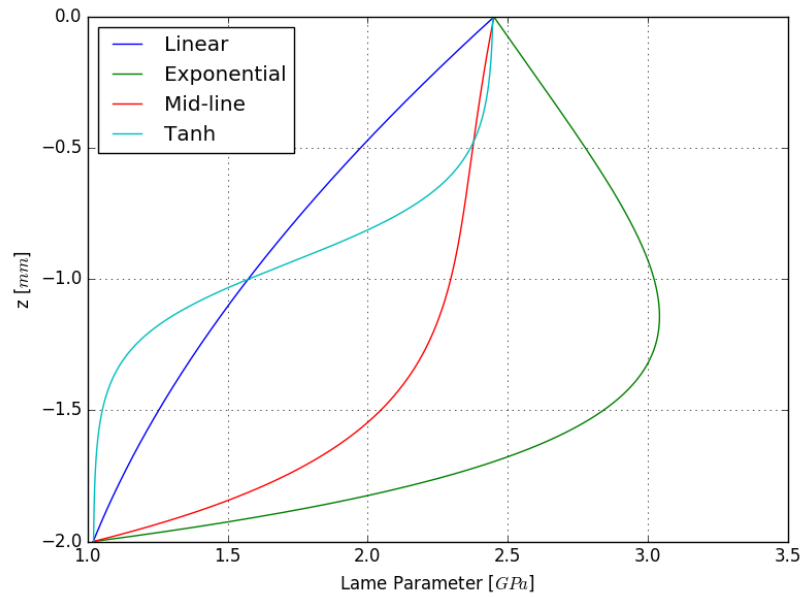
**Figure 3-13:** The four models of how the Bulk modulus varies with depth for the fluid-mud layer



**Figure 3-14:** The four models of how the Young's modulus varies with depth for fluid-mud.

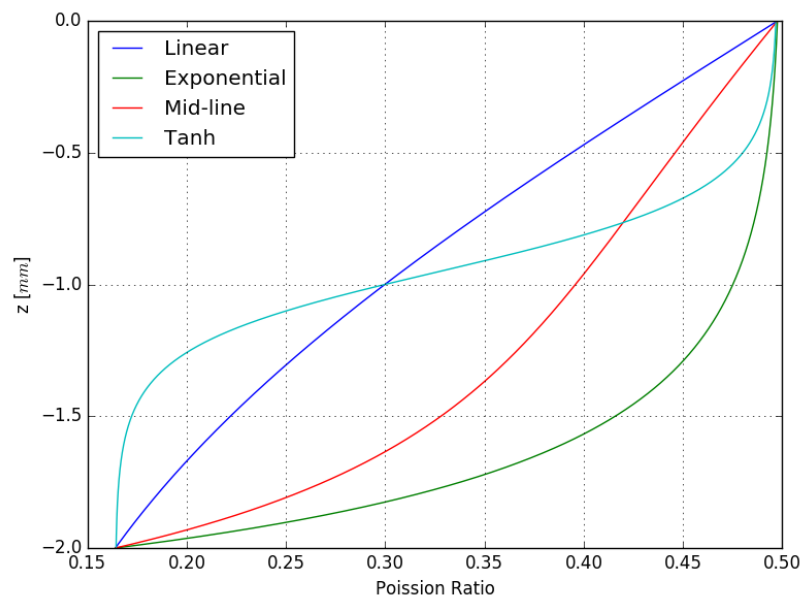
models. The linear, mid-line and tanh models all describe a decrease in the Lamé parameter. The exponential model shows an initial increase in the Lamé parameter followed by a sharp decrease. This is due to the prediction that the bulk modulus will increase for shallow depth and the fact the shear modulus varies only a small amount for shallow depths.

Figure 3-16 displays how the Poisson ratio varies with depth. All models show a decrease in the Poisson ratio with depth. The Poisson ratio describes the ratio of transverse strain to



**Figure 3-15:** The four models of how the Lamé's first parameter varies with depth for fluid-mud.

axial strain, meaning it describes how the material will expand in directions perpendicular to the direction of compression. The upper limit is 0.5 for water; sandstone has a Poisson ratio of 0.2.



**Figure 3-16:** The four models of how the Poisson ratio varies with depth for fluid-mud.

Figure 3-17 displays how the P-wave modulus varies with depth. All four models show an increase in P-wave modulus with depth.

The results and implications of the modelled parameters will be discussed more in the dis-

cussion section (Section 6-1).

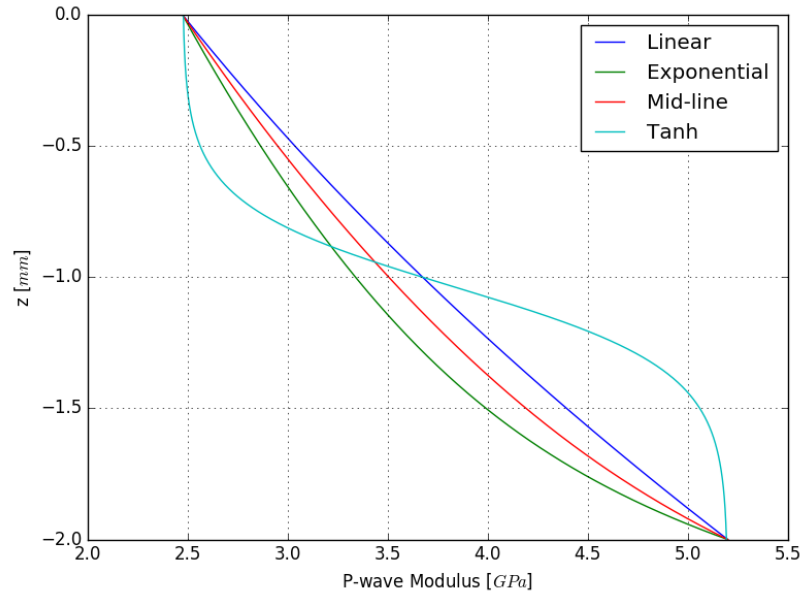


**Figure 3-17:** The four models of how the P-wave modulus varies with depth for fluid-mud.

## **Part IV**

# **Laboratory Experiments**



# Laboratory Experiments

## 4-1 Introduction

Three separate laboratory experiments were undertaken, each measuring the P-wave and S-wave velocities whilst changing a certain parameter. These measurements and parameters are:

- Velocity measurements of fluid-mud with varying density.
- Velocity measurements of fluid-mud for varying incident frequency.
- Velocity measurements of fluid-mud with time.

The results of these experiments will be displayed in the following results section (Section 5).

## 4-2 Velocity Measurements of PoR fluid-mud of varying density.

### 4-2-1 Introduction

The aims of the velocity measurements are to:

1. Investigate how the P-wave velocity varies with density for fluid-mud.
2. Investigate how the S-wave velocity varies with density for fluid-mud.

The fluid-mud sample was taken from the area known as 8e Petroleumhaven in the Maasvlakte part of the [PoR](#). The Maasvlakte is an area of the [PoR](#) which protrudes into the North Sea, an area reported by the [PoR](#) as having significant fluid-mud.

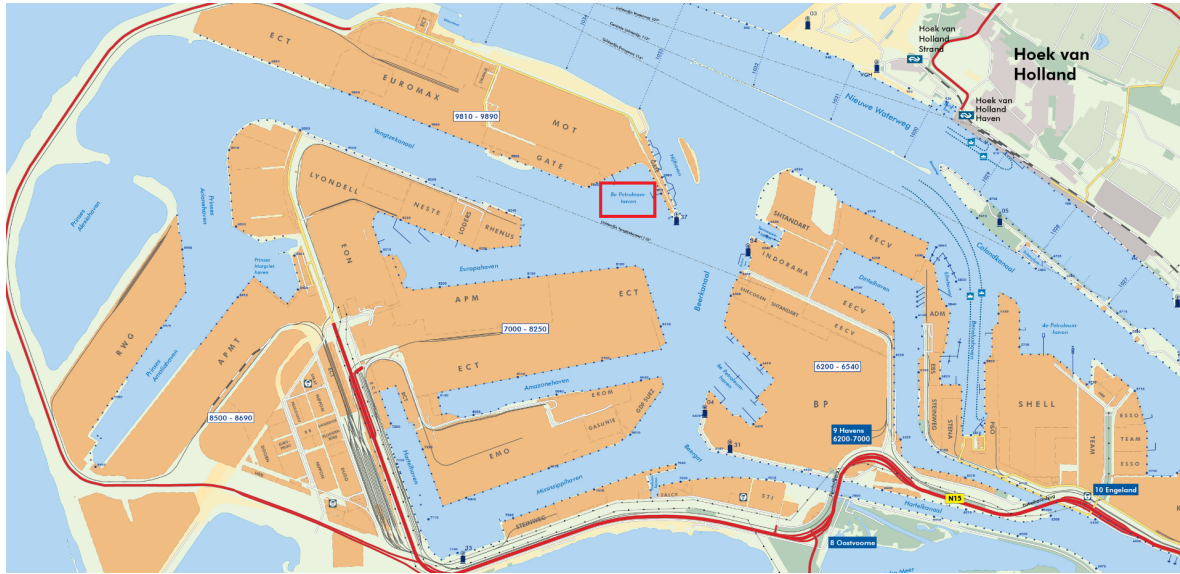


**Figure 4-1:** The location (red box) of 8e Petroleumhaven in the PoR of which the fluid-mud sample is taken from.

#### 4-2-2 Laboratory Setup

The P-wave and S-wave velocities were investigated for a variety of fluid-mud densities. The apparatus consisted of:

- A plastic container with dimensions  $11\text{cm} \times 16.8\text{cm} \times 14.2\text{cm}$ ;
- 4 1MHz Panametrics Transducers (two as sources and two as receivers);
- 1 Yokogawa DL9140 Digital Oscilloscope;
- 1 Agilent 33210A Function Generator;
- 1 RF Power Amplifier with trigger.

Four water-tight transducers are situated on the side walls of the plastic container. The placement of these are shown in Figure 4-2. The P-wave source and receiver transducers are situated opposite to each other, likewise with the S-wave transducers. The source transducers are connected to the waveform generator (via the power supply with trigger) when needed and the receiver transducers are connected to the oscilloscope. For example, when a P-wave measurement is undertaken, the P-wave source is connected to the waveform generator and a 1 MHz sine wave burst of amplitude  $0.75\text{ V}$  is produced. The produced wave travels through the fluid mud, is measured by the receiving transducer and visualised on the oscilloscope. The trigger provides a zero time stamp for the oscilloscope so that the received signal time is recorded correctly.

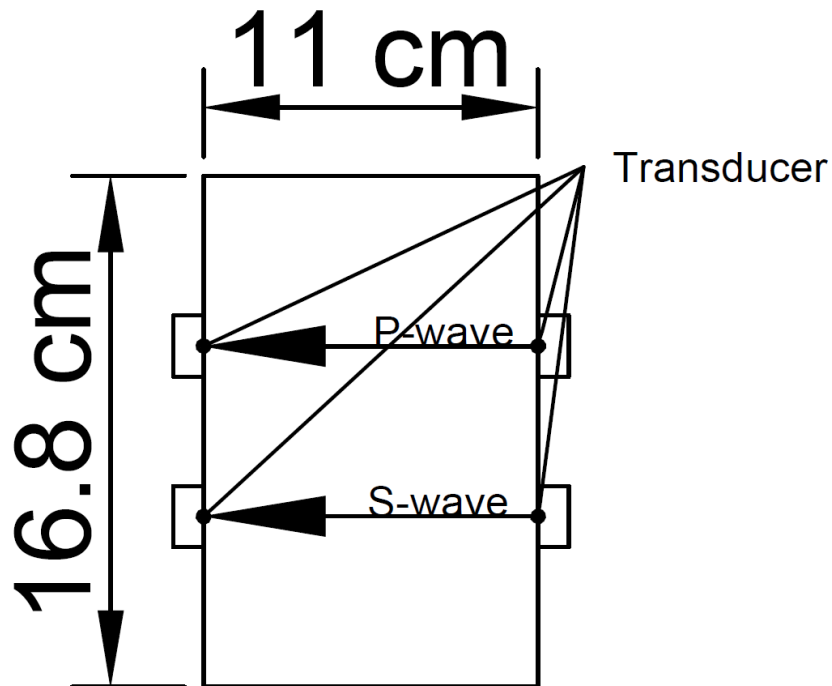


Figure 4-2: The laboratory setup for P-wave and S-wave velocity investigation.

### 4-2-3 Methodology

The methodology of the test procedure is as follows:

1. Consolidated fluid mud of a known mass and volume is placed in the apparatus.
2. A P-wave is generated by the source transducer and measured at the receiver transducer.
3. An S-wave is generated by the source transducer and measured at the receiver transducer.
4. The travel time for each wave is measured by the peak of the first arrival.
5. The fluid-mud is diluted by adding water in 100ml increments and stirred to make the fluid-mud as homogeneous as possible. For each increment, steps 2 - 4 are repeated.

## 4-3 The effects of frequency on wave velocity for the PoR fluid-mud.

### 4-3-1 Introduction

The aims of the frequency measurements are to:

1. Investigate how the P-wave velocity of the fluid-mud varies with the incident frequency.

### 4-3-2 Laboratory Setup

The experimental setup is the same as that described in Section 4-2-2 and shown in Figure 4-2.

### 4-3-3 Methodology

The methodology of the test procedure is as follows:

1. Consolidated fluid mud of a known mass and volume is placed in the apparatus.
2. Waveforms of frequencies from  $1.2MHz$  to  $100kHz$  in  $100kHz$  decrements and from  $100kHz$  to  $10kHz$  in decrements of  $10kHz$  are produced by the waveform generator.
3. A P-wave is generated by the source transducer and measured at the receiver transducer for each frequency increment.
4. The travel time is measured by the peak of the first arrival for each frequency increment.

## 4-4 Effects of time on the seismic/rheological properties of PoR fluid-mud

### 4-4-1 Introduction

The aims of the time-velocity measurements are to:

1. Investigate how the P-wave and S-wave velocity of the fluid-mud varies with time.
2. Investigate how the density of the fluid-mud varies with time.
3. Investigate how the P-wave reflection coefficient of the water-fluid-mud contact varies with time.
4. Investigate how the shear modulus, bulk modulus and other elastic properties of the fluid-mud vary with time.

### 4-4-2 Laboratory Setup

The experimental setup is the same as that described in Section 4-2-2 and shown in Figure 4-2.

### 4-4-3 Methodology

The methodology of the test procedure is as follows:

1. Fluid mud of a known mass and volume is placed in the apparatus.
2. A P-wave is generated by the source transducer and measured at the receiver transducer.
3. A S-wave is generated by the source transducer and measured at the receiver transducer.
4. The travel time for each wave is measured by the peak of the first arrival.
5. The fluid-mud is left undisturbed for a period of time. As the fluid-mud begins to dewater, the height of the water and fluid-mud interfaces are measured. From this, the density of the fluid mud can be calculated (assuming the water has a density of  $1000 \text{ kg.m}^{-3}$ ).
6. Steps 2-5 are repeated after different periods of time allowing more dewatering of the fluid-mud.



**Part V**

**Results**



### 5-1 Velocity - Density

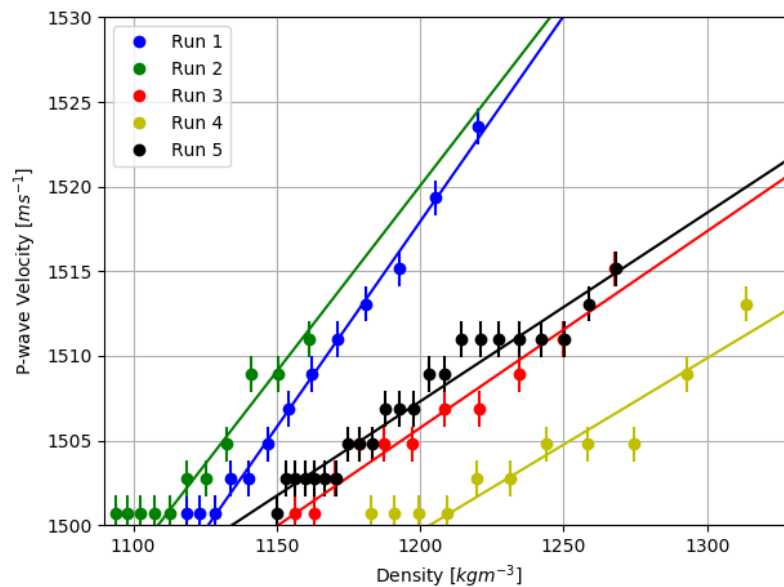


**Figure 5-1:** The results of the velocity measurements on the PoR fluid-mud of varying density.

The experiment ran five times, with the P-wave velocity results shown in Figure 5-1. Unfortunately, it was not possible to unambiguously pick S-wave first arrivals due to a large amount of noise and P-wave arrivals masking the S-wave arrivals. All the experimental data act asymptotically at  $1500 \text{ m}\cdot\text{s}^{-1}$  for low densities before increasing linearly above a certain density. Note that the change from the asymptotic to linear behaviour happens at a variety of densities. Lines of best fit have been fitted for the data that has the linear behaviour. The results will be further discussed in Section 6-2.

## 5-2 Velocity - Frequency

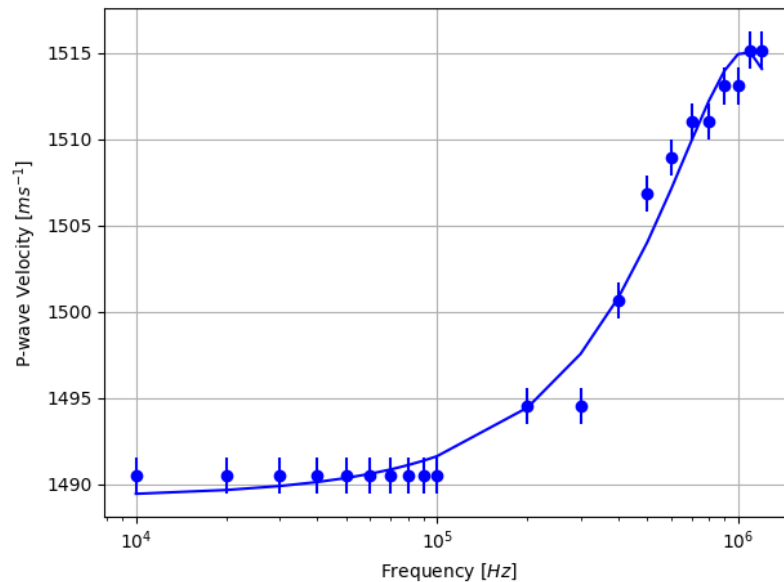


**Figure 5-2:** The results of the velocity measurements on the PoR fluid-mud of varying frequency.

Below a frequency of 100 *kHz* the P-wave velocity measured acts asymptotically and gives a reading of approximately 1490 *m.s*<sup>-1</sup>. Above a frequency of 100 *kHz*, the measured velocity increases in a logarithmic manner until it levels asymptotically at approximately 1.1 *MHz*. The results will be discussed further in Section 6-3.

## 5-3 Velocity - Time

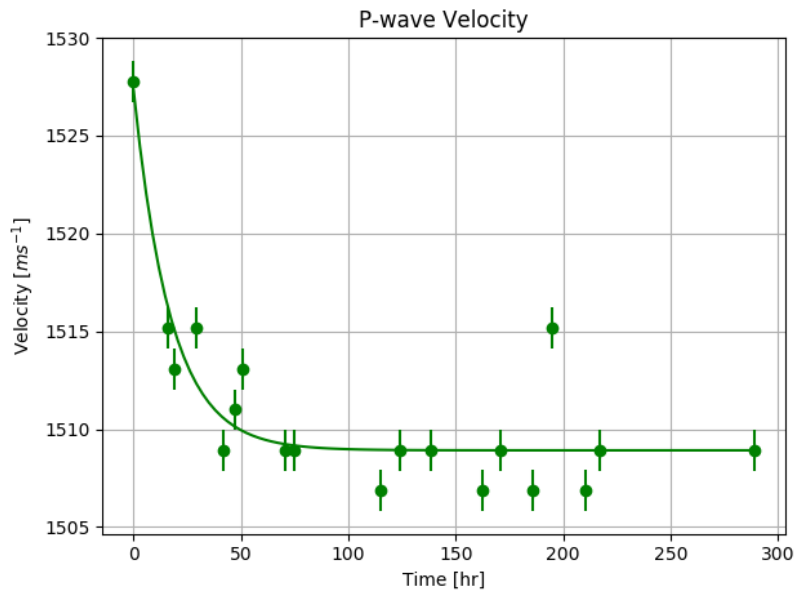
We can see in Figure 5-3 that the P-wave velocity shows an exponentially decaying behavior. The gradient is initially negative and large for early times, the negative gradient then decreases with time. The reason for the decrease in P-wave velocity and further analysis will be discussed in Section 6-4-1.

Figure 5-4 shows a logarithmic increase in S-wave velocity with time starting from a velocity of zero at time zero and an asymptote of approximately 1000 *m.s*<sup>-1</sup>. More about these results in Section 6-4-2.

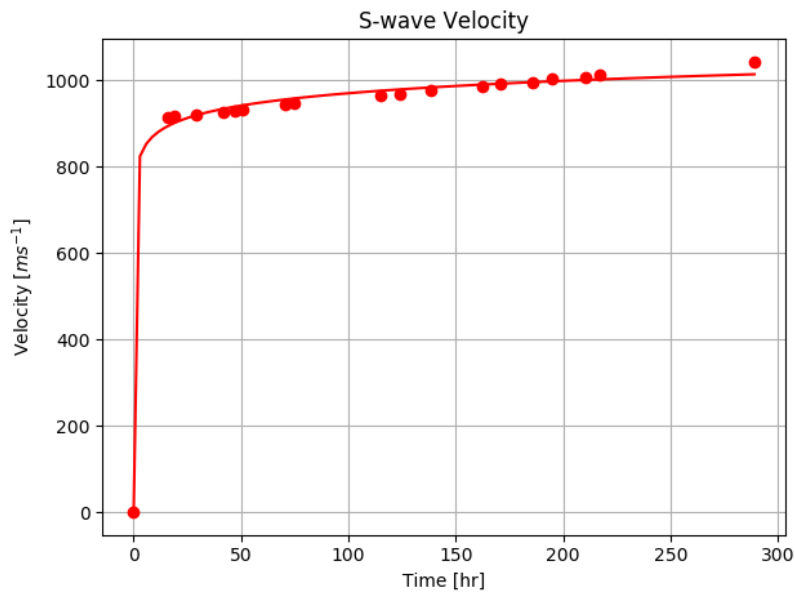
Figure 5-5 initially demonstrates a logarithmic increase of density with time. At later times the rate of density increase slows. The empirical formula derived for the change in density is  $\rho = 43 \ln(t + 18) + 1038$ . The discussion of the results can be found in Section 6-4-3.

Figure 5-6 demonstrates how the P-wave reflection coefficient changes with a change in density of the fluid-mud. This relationship demonstrates a linear trend described by  $R = 3.5 \times 10^{-4} \rho - 0.32$ . The implications will be discussed further in Section 6-4-5.

Because the S-wave velocity and density is known, the shear modulus can be calculated. Likewise with the bulk modulus - by knowing the shear modulus, density and P-wave velocity.



**Figure 5-3:** The results of the P-wave velocity measurements on the PoR fluid-mud with increasing time.



**Figure 5-4:** The results of the S-wave velocity measurements on the PoR fluid-mud with increasing time.

How both moduli vary with time and density is shown in Figures 5-7 and 5-8, respectively. We can see that the bulk modulus decreases initially unlike the shear modulus, which increases initially. The bulk modulus appears to have a slightly steeper gradient than the shear modulus. Both then trend asymptotically to a modulus of approximately  $1.25 \text{ GPa}$ . A good description of the plot is that a mirror has been placed at the asymptote of  $1.25 \text{ GPa}$  and the shear

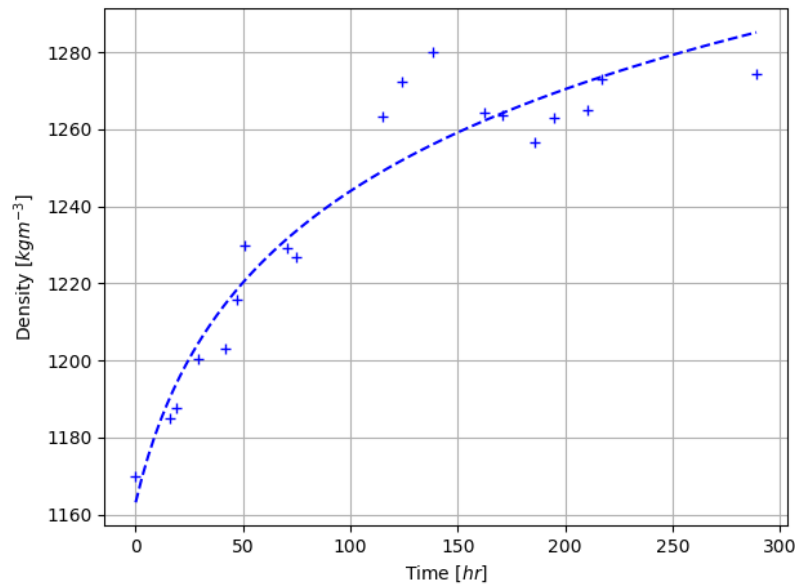


**Figure 5-5:** A graph to show how density changes with time for the PoR fluid-mud.

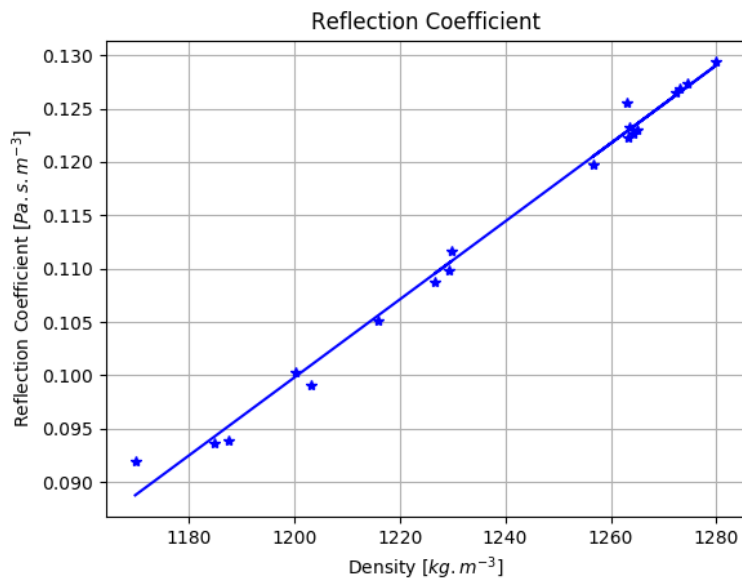


**Figure 5-6:** A graph to show how P-wave reflection coefficient changes with time for the PoR fluid-mud.

and bulk modulus mirror each others behaviour. At a time of approximately 165 hours of consolidation, or at a density of  $1260 \text{ kg.m}^{-3}$ , the shear modulus becomes higher than the bulk modulus, meaning that the shear modulus becomes the more dominating modulus. The bulk modulus of water is approximately  $2.25 \text{ GPa}$ , the initial starting bulk modulus of the fluid-mud is slightly above that at  $2.6 \text{ GPa}$  because of the higher density of the solution with the fluid-mud particles suspended in it. These results will be discussed further in Section 6-4-6.

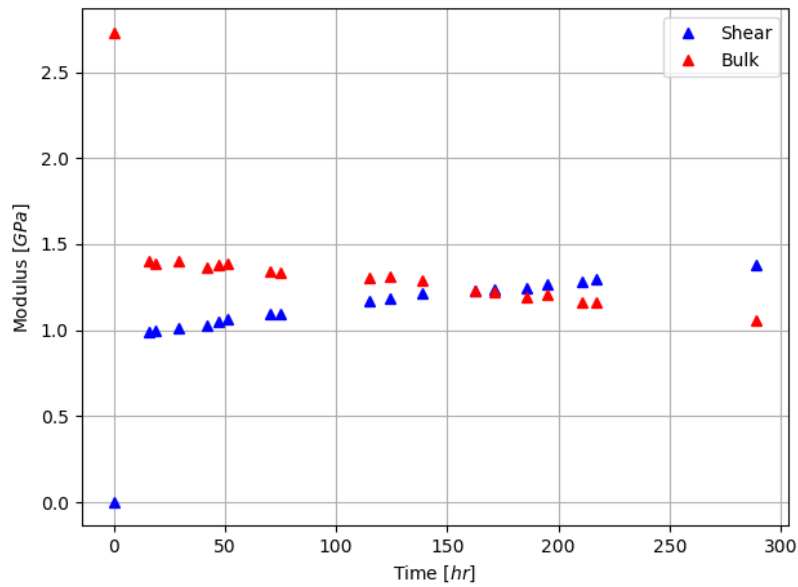


Figure 5-7: A graph to show how the shear and bulk modulus change with time for the PoR fluid-mud.

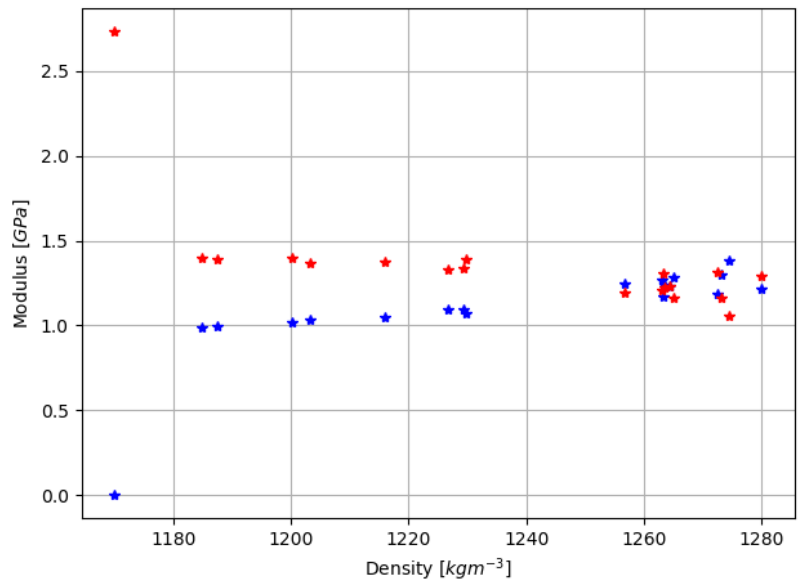
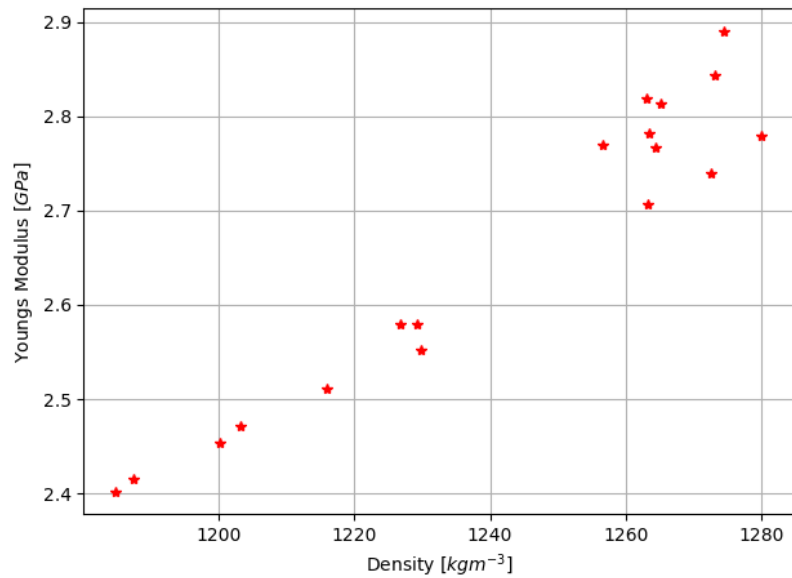


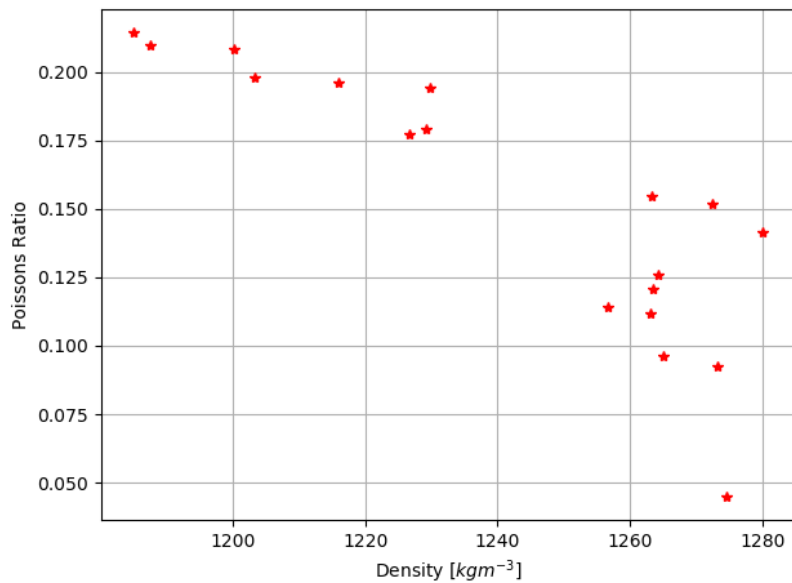
Figure 5-8: A graph to show how the shear and bulk modulae change with density for the PoR fluid-mud.

Figure 5-9 shows the calculated Young’s modulus for the corresponding fluid-mud density, the point of zero time has been neglected. The Young’s modulus ranges from between 2.4 and 3 GPa and increases linearly with the fluid-mud density.

Figure 5-10 displays the calculated Poisson’s ratio for a change in fluid-mud density. The trend of the data is that the Poisson’s ratio decreases exponentially for an increase in density.



**Figure 5-9:** A graph to show how the Young's modulus changes with density for the PoR fluid-mud.



**Figure 5-10:** A graph to show how the Poisson's ratio changes with density for the PoR fluid-mud.

The values of the Poisson's ratio range from 0.05 to 0.225.

Figure 5-11 presents the calculated first Lamé parameter and how it varies for a change in fluid-mud density. The Lamé parameter decreases exponentially with a decrease in density with values ranging from 0.1 - 0.8 GPa.

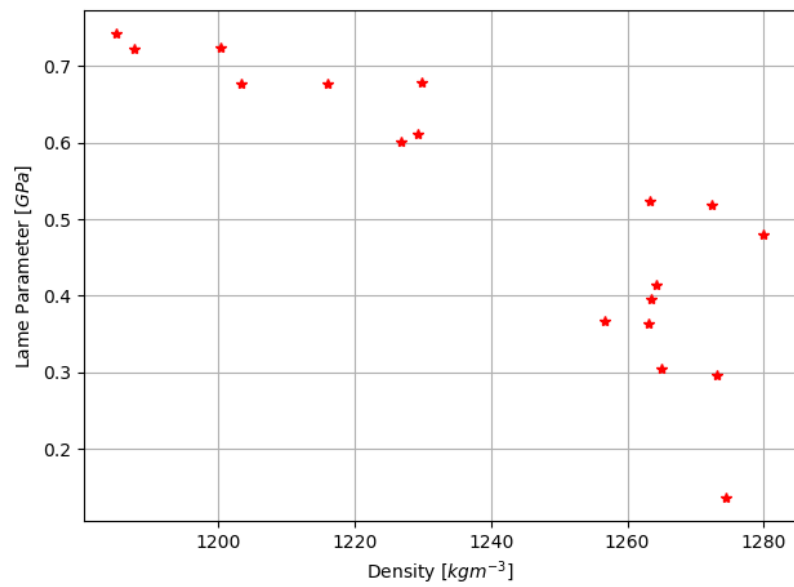


**Figure 5-11:** A graph to show how the first Lamé parameter changes with density for the PoR fluid-mud.



**Part VI**

**Discussion**



---

# Chapter 6

---

## Discussion

### 6-1 Modelling

Modelling an expected water, fluid-mud and solid system for varying source and receiver height showed a dependency on the height on the ability to detect converted PS-waves and Scholte-waves, both of which are crucial for deriving rheological properties of the fluid mud. It was shown that the source and receivers needed to be less than 2 m away from the fluid-mud interface.

It is promising that the PS conversions and Scholte wave can be detected on the modelled data but real data is expected to have noise, P-wave reflections from layers below the fluid-mud and an unknown geometry. Therefore, it is expected that the raw field data will need to be pre-processed to interpret waves of value. A field experiment is suggested for this. If an accurate and clear seismic record can be obtained from a survey in the [PoR](#), the P-wave and S-wave velocities of the fluid-mud can be estimated. Two scenarios are proposed:

1. The P-wave and PS-wave reflections are visible, in which an NMO correction can be applied to the seismic section and the resulting P-wave and S-wave velocities obtained.
2. The P-wave and Scholte-wave reflections are visible. This implies that the P-wave velocity can be calculated by applying NMO correction and the Scholte-wave velocity can be determined by the gradient of the event on the seismic section. The S-wave velocity can then be obtained by methods described in [Section 2-4](#).

Assuming the P- and S-wave velocity can be estimated from the seismic section, the shear and bulk modulus could be calculated. This gives an indication of the incompressibility and stiffness of the fluid-mud, respectively. Both these parameters exist for fluid-mud as confirmed by laboratory measurements, which are shown in [Figure 5-7](#), and could provide the basis for a new nautical-depth level.

Knowing the shear and bulk modulae allowed for the estimation of the elastic constants when the fluid-mud was assumed to respond elastically under small stresses. Because both the shear



and bulk modulus had been measured, in later laboratory measurements, for the fluid-mud it must be so that the elastic constants are meaningful. The Young's modulus combined with the shear modulus can give detailed information about the stiffness of the fluid-mud. This is because the Young's modulus describes the response of a material to linear strain while the shear modulus is the response to shearing strain.

The Poisson's ratio could allow for actual calculation of the stress-strain curve for the fluid-mud, allowing the yield point of the fluid-mud to be found, using the assumption that the fluid-mud obeys Hooke's law. This would be very useful for determining a new nautical depth for the **PoR** because if the yield point is known, then the stress needed to be induced on the mud for it to be out of its elastic range and into plastic deformation can be derived. This effectively shows how much stress the ship would have to put on the fluid-mud for it to become a fluid again.

If the properties of the top and bottom of the fluid mud can be determined then four models have been discussed on how rheological parameters and elastic constants profiles may vary with depth. These have been based on previous literature studies and thoughts of the author. The behaviour of fluid-mud needs to be studied further in order to justify these claims and how the fluid-mud reacts to larger stresses.

## 6-2 Velocity Measurements

Figure 5-1 shows the results of the velocity measurements. All the plots show the same asymptotic trend to  $1500 \text{ m.s}^{-1}$  at low densities with a then linear behaviour of varying gradients as density increases. The difference in gradients seem to correspond to how disturbed the fluid-mud was. Run one and two were for consolidated mud that had been left in the lab for some period of time. Care was taken not to disturb the fluid-mud sample. The mud had been considerably disturbed for runs three, four and five. This could be the reason why runs one and two have similar gradients, likewise with runs three, four and five.

The lines of best fit for runs one, two, three and 5 all cross the asymptote  $1500 \text{ m.s}^{-1}$  in the range of  $1100$  to  $1150 \text{ kg.m}^{-3}$ .

Because water is being added to the fluid-mud for each measurement, the fluid-mud is getting agitated each measurement and therefore not being allowed to settle. It is apparent that this measurement is most likely to be more representative of the change in P-wave velocity with change in concentration of fluid-mud suspended in water. Therefore, we see a decrease in P-wave velocity as the fluid-mud becomes less concentrated/more saturated with water. In the experiment that investigates how the P-wave and S-wave velocity changes with time, the density has been derived and therefore is a more accurate measurement for how the velocities change with density.

## 6-3 Frequency Measurements

Figure 5-2 shows that high frequencies result in a higher P-wave velocity. This is most likely due to an increased reaction with the fluid-mud particles. With a higher frequency, the probability of a P-wave being incident on a fluid-mud particle is higher. Frequencies above

1MHz truly represent the velocity of the fluid-mud because the P-waves at these frequencies are interacting with the suspended fluid-mud and therefore are more sensitive to change. The reason behind the asymptote at lower frequencies (below 100 kHz) is that the P-waves are no longer interacting with the with fluid-mud particles and provide no information about the fluid-mud.

The dimensions of this experiment are small in comparison to the thickness of the fluid-mud layer in the port. It is well know that with seismic acquisition there is a trade off between frequency and penetration depth. Therefore, whilst the higher frequencies will provide the most accurate and sensitive response to changes in the fluid mud, they are also attenuated the quickest. Therefore, there is a trade off between frequency and penetration depth and this would need to be investigated for fluid-mud.

## 6-4 Effects of time on the seismic and rheological properties of fluid-mud

### 6-4-1 P-Wave Velocity

The effects of time on the P-wave velocity of fluid-mud from the PoR is displayed in Figure 5-3. The trend of the P-wave velocity is an exponential decay with time. One reason behind this decay could be that as the fluid-mud de-waters, air bubbles are trapped within the fluid mud. With air having a low bulk modulus, the P-wave velocity is reduced. Empirically a line of best fit was plotted as  $V_p = 18e^{-0.058t} + 1509$  which matched the data well.

### 6-4-2 S-Wave Velocity

The value of S-wave velocity at zero time (Figure 5-4) is an issue to discuss. The measurement could well be zero, which is what we expect for water with no shear modulus. However because the fluid-mud is suspended in the water, some rigidity may be expected. The shear modulus value may be so small that the S-wave amplitude is also very small and masked by noise. Therefore some caution must be taken with this first measurement. If we assume the S-wave velocity is zero at zero time then the S-wave velocity appears to increase logarithmically with time. A logarithmic line of best fit was fitted to the data with the empirical formula  $V_s = 36 \ln(t + 2.8 \times 10^{-10}) + 785$ . If it is assumed that the fluid-mud has some rigidity at zero time then a linear relationship can be plotted for the increase in S-wave velocity with time.

### 6-4-3 Density

Density logarithmically increases with time (Figure 5-5). Empirically the relationship was deduced to be  $\rho = 43 \ln(t + 18) + 1038$ . The increase in density is thought to be due to de-watering and consolidation of the fluid-mud. The data presented here suggests that for a time scale of a few days these processes cause the density to increase linearly with time, then slowing down at larger times.

During the experiment initial results of density lead to an over calculation of the density with higher values that expected. This is because the system was assumed to be a closed system

but in reality there is also evaporation of the water that sits on top of the fluid mud. At a later stage in the experiment, when the fluid-mud interface was decreasing in height at a very slow rate, an estimate of the evaporation rate was made. This evaporation rate was deduced to be  $1 \times 10^{-6} \text{ m}^3.\text{hr}^{-1}$  which lead to density values consistent with [Shahmirzadi et al. \(2016\)](#), [Ha et al. \(2010\)](#).

The results are assuming that the fluid-mud is homogeneous and has the same structure throughout. However one should hypothesise that there is an internal density profile within the mud, with the top of the fluid-mud has a lower density than the bottom [Shahmirzadi et al. \(2016\)](#). This is thought to be due to compaction from the pressure of the weight above the mud at the bottom and sorting of grains.

That fact that a density profile exists within the fluid-mud is positive for the use of reflected waves to determine the rheological properties. This means there will be a change in acoustic impedance and therefore a reflected seismic waves with varying amplitudes.

#### 6-4-4 Fluid-mud Interface

Promisingly the fluid-mud interface acted exponentially as stated by [Ha et al. \(2010\)](#) & [Maa et al. \(1997\)](#). The consolidation and settling of fluid-mud can be split into three stages:

1. The first few hours the fluid-mud interface (initial value being the height of the water/fluid-mud mix) rapidly drops at a high settlement rate;
2. Between 28 and 186 hours the consolidation and settling continued at a moderate rate, with the interface height reflecting that;
3. After 186 hours the consolidation and settling rate continued at a very slow rate.

These three stages are shown in Figure 6-1 in red, yellow and green respectively. The experimental system was obviously a closed system with regards to the fluid-mud. There were no source or sinks of the fluid-mud, meaning there could not be an increase or decrease in the amount of fluid-mud within the system. This would not be the case in the [PoR](#) because fluid-mud would be being deposited and eroded with time.

#### 6-4-5 Reflection Coefficient

P-wave reflection coefficient increases linearly with density with the empirical relationship  $R = 3.7 \times 10^{-4} \rho - 0.3$ . This demonstrates that as the fluid-mud is allowed to settle and consolidate, the reflections from the fluid-mud will become stronger as a greater proportion of the P-wave is reflected. This establishes that the longer the fluid-mud is left undisturbed and therefore the higher the density, the more accurate and reliable a seismic survey of the fluid mud will be. This is because the reflections will become stronger and therefore parameters such as first arrivals and amplitudes will be easier to pick. This relationship derived here could provide quick and easy density profiling by just analysing the signal strength of the reflections.

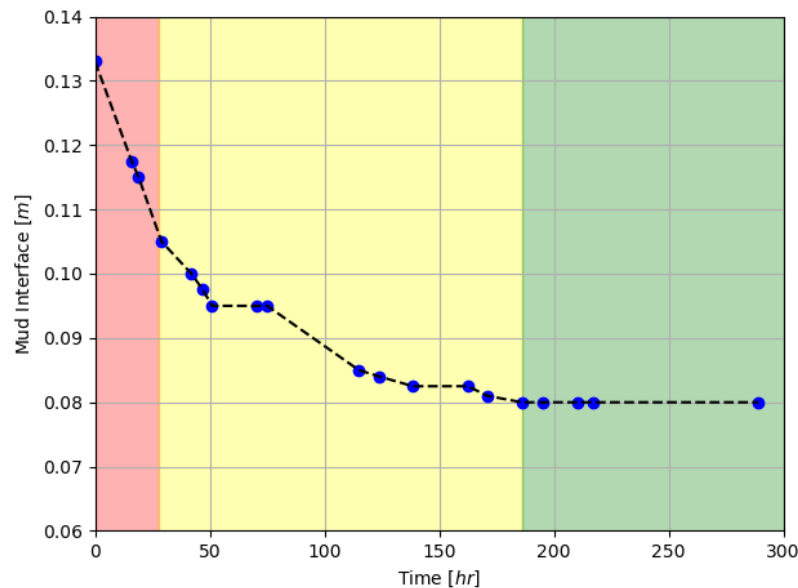


**Figure 6-1:** A graph to show how the height of the PoR fluid-mud interface changes with time. Red = stage 1, Yellow = stage 2 and Green = stage 3.

#### 6-4-6 Shear & Bulk Modulus

At a time of zero, the S-wave velocity is zero (Figure 5-4) and therefore the shear modulus is also zero (Figure 5-7). This means the P-wave velocity is solely dependent on the bulk modulus. The bulk modulus at time zero was deduced to be  $2.6 \text{ GPa}$  this is above the bulk modulus of water, which is  $2.25 \text{ GPa}$  meaning that the suspended fluid-mud particles add some loose structure to the water. As the fluid mud settles and consolidates the bulk modulus decreased exponentially and the shear modulus increases logarithmically (Figure 5-7). At a time of 160 hours the shear modulus becomes greater than the bulk modulus. This could mean that the shear strength becomes the more dominant strength of the fluid-mud, whereas it was incompressibility before this time.

Shear strength of the fluid mud is a property that could be used to define the nautical depth of the PoR. The shear strength defines how much resistance the fluid-mud will apply to a vessel that is sailing through it. The values of shear modulus presented in this paper should be verified but provided the basis for accurate in-situ shear modulus and shear strength determination.

#### 6-4-7 Elastic Constants

The Young's modulus, Lamé's first parameter and Poisson's ratio could be derived from the seismic velocities. The Young's modulus demonstrated a linear behaviour with density and time, whereas the Lamé's parameter and Poisson's ratio decreased exponentially with density and time. The Young's modulus increased with density/time which represents a materials increase in stiffness, which is exactly what is expected of fluid-mud as it consolidates and settles. The Poisson ratio decreases exponentially with density/time, meaning that the ratio

of transverse strain to axial strain is decreasing. This means that as a transverse strain applied to the fluid-mud of a lower density will cause a larger axial deformation than that of a fluid-mud of higher density. Lamé's first parameter has no physical meaning but is used to derive stress-strain relationships when combined with the shear modulus. This could be a point of further research at this stage to clarify if the assumption that the fluid-mud can be treated as an elastic and Hookean material is correct. If so it could form the basis of finding the yield point of the fluid-mud which would be invaluable in defining a new nautical depth.

## **6-5 Further Research**

### **6-5-1 Viscosity Determination**

The determination of viscosity from reflected seismic waves would have been ideal but was beyond the scope of this thesis. However this is theoretically possible from reflected seismic waves in reservoir sandstones as described by [Best and McCann \(1995\)](#) . The reflection from the water-fluid mud interface will have a higher amplitude than the fluid mud-solid interface. The change in quality factor/ seismic attenuation can be attributed to a change in viscosity via the Biot theory. This theory would need to be tested for fluid-muds but it is hoped that it can be extended/adapted for the use of viscosity determination of fluid-mud.

## **Part VII**

# **Conclusion**



---

## Chapter 7

---

# Conclusion

Reflected seismic waves show great potential in deriving in situ rheological and elastic parameters of fluid-mud from the [PoR](#). If accurate P-wave velocity, S-wave velocity and fluid-mud density can be derived from the reflected waves, then many advantageous parameters can be derived and used to define a more suitable nautical depth for the [PoR](#). These parameters include: shear modulus, bulk modulus, Young's modulus, Lamé's first parameter and Poisson's ratio. In situ values of these parameters have been measured for fluid-mud from 8e Petroleumhaven in the [PoR](#) and need to be independently verified by other measurements methods. If verified, empirical formulation could be used for quick parameter determination. Modelling demonstrated that converted PS waves and the Scholte wave can be detected for offsets smaller than 2 m, a promising result for quick data acquisition over large areas of the port. Field measurements are recommended to deduce the most suitable frequency for data acquisition, with the trade off between resolution and penetration depth of the fluid-mud needing to be optimized. Results from experiments on the fluid-mud yielded 1.1 *MHz* as the top limit of sensitivity and 100 *kHz* as the lowest. Viscosity determination could also be possible with the use of the quality factor determined from reflected seismic waves and an investigation into this is recommended.



---

# Bibliography

- Best, A. I. and McCann, C. (1995). Seismic attenuation and porefluid viscosity in clayrich reservoir sandstones. *GEOPHYSICS*, 60(5):1386–1397.
- Birch, F. (1961). The velocity of compressional waves in rocks to 10 kilobars: 2. *Journal of Geophysical Research*, 66(7):2199–2224.
- Bohlen, T., Kugler, S., Klein, G., and Theilen., F. (2004). 1.5d inversion of lateral variation of scholte-wave dispersion. *Geophysics*, 69(2):330–344.
- Drijkoningen, G., el Allouche, N., Thorbecke, J., and Bada, G. (2012). Nongeometrically converted shear waves in marine streamer data. *Geophysics*, 77(6):45–56.
- Fontein, W. and Byrd, R. (2007). The nautical depth approach, a review for implementation. *WODA Florida*.
- Fontein, W. and van der Wal, J. (2006). Assessing nautical depth efficiently in terms of rheological characteristics. *International Hydrographic Conference*.
- Ha, H. K., Maa, J. P.-Y., and Holland, C. W. (2010). Acoustic density measurements of consolidating cohesive sediment beds by means of a non-intrusive “micro-chirp” acoustic system. *Geo-Marine Letters*, 30(6):585–593.
- Hamilton, E. L. (1971). Elastic properties of marine sediments. *Journal of Geophysical Research*, 76(2):579–604.
- Hwang, K., Mehta, A., of Florida. Coastal, U., Department, O. E., and (Fla.), S. F. W. M. D. (1989). *Fine Sediment Erodibility in Lake Okeechobee, Florida*. Coastal & Oceanographic Engineering Department, University of Florida.
- Jia, R., Hino, T., Chai, J., Hamada, T., and Yoshimura, M. (2013). Interpretation of density profile of seabed sediment from nuclear density cone penetration test results. *Soils and Foundations*, 53(5):671 – 679.

- Kaya, A., Yoshida, H., Tanigawa, H., Igata, H., and Tsuruya, H. (2008). Chapter 2 estimation of sea bottom density profile through analysis of ultrasonic echo signals. *Proceedings in Marine Science*, 9:17 – 30. Sediment and Ecohydraulics.
- Maa, J. P.-Y., Sun, K.-J., and He, Q. (1997). Ultrasonic characterization of marine sediments: a preliminary study. *Marine Geology*, 141(1):183 – 192.
- McAnally, W. H., Teeter, A., Schoellhamer, D., Friedrichs, C., Hamilton, D., Hayter, E., Shrestha, P., Prodriguez, H., Sheremet, A., and Kirby, R. (2007). Management of fluid mud in estuaries, bays and lakes. ii: Measurement, modelling and management. *Journal of Hydraulic Engineering*, 133(1).
- Mehta, A. J., Samsami, F., Khare, Y. P., and Sahin, C. (2014). Fluid mud properties in nautical depth estimation. *Journal of Waterway, Port, Coastal, and Ocean Engineering*, 140(2):210–222.
- Park, C. B., Miller, R. D., Xia, J., Ivanov, J., Sonnichsen, G. V., Hunter, J. A., Good, R., Burns, R., and Christian, H. (2005). Underwater MASW to evaluate stiffness of water-bottom sediments. *The Leading Edge*, 24(7):724–728.
- Scholte, J. (1958). Rayleigh waves in isotropic and anisotropic elastic media. *Mededelingen en verhandelingen*, 72.
- Shahmirzadi, M., Staelens, P., S.Claeys, H.Cattrysse, Hoestenbergh, T. V., Oyen, T. V., Vanlede, J., T.Verwaest, and F.Mostaert (2016). Experimental investigation on consolidation behavior of mud: Subreport 2 - factual data report.
- Thorbecke, J. and Draganov, D. (2011). Finite difference modelling for seismic interferometry. *Geophysics*, 76(5):H1 – H18.
- Vinh, P. C. (2013). Scholte-wave velocity formulae. *Wave Motion*, 50(2):180 – 190.